

Synergistic electronic structure modulation in single-atomic Ni sites dispersed on Ni nanoparticles encapsulated in N-rich carbon nanotubes synthesized at low temperature for efficient CO₂ electrolysis

Ramireddy Boppella ^{a,b}, Youngsam Kim ^a, K. Arun Joshi Reddy ^a, Inae Song ^a, Yaaeun Eom ^a, Eunji Sim ^{a,*}, Tae Kyu Kim ^{a,*}

^a Department of Chemistry, Yonsei University, Seoul 03722, the Republic of Korea

^b Department of Mechanical Engineering, Colorado State University, Fort Collins, CO 80526, USA



ARTICLE INFO

Keywords:

Single atom catalyst
Nanoparticle
N-doped carbon
CO₂ reduction
Electrocatalyst

ABSTRACT

Ni, N-doped carbon materials (Ni–N–C) are prosperous candidates for the electrochemical CO₂ reduction reaction (CO₂RR) due to their outstanding activity and selectivity. However, the role of the coexisting uncoordinated N-doped sites and Ni nanoparticles (Ni-NPs) in overall CO₂RR has been overlooked in prior studies. To address this gap, a low temperature synthesis method developed for Ni-NP-encapsulated Ni–N–C nanotube (Ni-NCNT) catalysts with atomically dispersed Ni–N₄ and abundant uncoordinated N-doped sites, where Ni-NPs increase the electron density on Ni–N–C nanotube through carbon network and synergistically enhances the CO₂RR activity. The systematic analysis reveals the cooperative role of Ni-NPs and uncoordinated N-doped sites in altering the electronic structure of Ni–N₄ sites. The results of control experimental studies confirm the synergistic interaction of uncoordinated N-doped sites boost the CO₂RR activity of Ni–N₄ sites. Additionally, density functional theory calculations show that the strong interaction between the Ni-NPs and Ni–N–C did not affect the electronic structures of the Ni–N₄ centers, but rather alter the electronic structure of uncoordinated pyridinic-N sites. This variation led to decreased the energy barriers of rate-limiting steps of COOH* formation on Ni–N₄ and N-doped sites, resulting in excellent CO₂RR performance.

1. Introduction

The electroreduction of CO₂ (CO₂RR) into value-added chemicals utilizing intermittent renewable energy sources, such as wind, solar, and geothermal energy, represents a viable solution for problems related to global warming and energy constraints. This approach is an ideal strategy for storing renewable electricity in chemical bonds [1–4]. In recent years, researchers have endeavored to develop electrocatalysts that are active and selective for the CO₂ reduction reaction (CO₂RR) while concurrently suppressing the competing hydrogen evolution reaction (HER). Currently, the most effective electrocatalysts for CO₂ reduction to CO are atomically dispersed active metal species anchored to the N sites of a N-doped carbon (N–C) framework (M–N–C) [5,6]. Among these species, the Ni–N – C framework has garnered the most attention for selective CO production [7,8]. Nevertheless, it is crucial to further investigate the Ni–N–C catalyst to achieve production levels that are acceptable for commercialization, while minimizing the competing

HER and avoid large overpotentials.

In general, to increase the CO₂RR activity, numerous active sites are required to work together in the catalytic process and efficiently adsorb and activate the substrate. In the case of CO₂RR, the nitrogen atoms coordinated to the metal atom (M–N_x) in M–N–C catalysts serve as an active site due to the appropriate reaction free energy between the M–N_x sites and reaction intermediates (COOH* and CO*) [9–11]. Along with the M–N_x sites, the presence of metal nanoparticles (M NPs) and N-doped species in M–N–C catalysts may affect the catalytic activity by altering the electronic configuration of M–N_x centers [12–14]. Specifically, N-doped species in carbon matrix (N–C) have been recognized as a potential active site for assisting selective CO₂RR [15–17]. However, the catalytic function of uncoordinated N-doped species in conjunction with M–N_x sites in M–N–C toward the CO₂RR remains largely unexplored [7,18]. One potential reason for this is that high-temperature pyrolysis dramatically decreased the N-doped content, introduces intrinsic defects in the carbon plane [18–20], and changes the

* Corresponding authors.

E-mail addresses: esim@yonsei.ac.kr (E. Sim), tkkim@yonsei.ac.kr (T.K. Kim).

coordination structure of the M–N_x centers from M–N₄ to M–N₃ and/or M–N₂, which are presumed to be more active than M–N₄ for CO₂RR [21–24]. Therefore, it remains challenging to elucidate the role of N-doped species in M–N–C catalysts due to the difficulty in synthesizing M–N–C catalysts with abundant N-doped species without altering the coordination structure of the isolated M–N_x sites. Hence, it is desirable to develop low-temperature synthesis strategies to create single atom catalysts.

Although the M NPs in M–N–C catalysts are well-known active sites for HER, they are strictly avoided during M–N–C catalyst synthesis, and the definition of their role remains controversial [12,25]. Notably, M NPs protected by carbon layers directly catalyze neither CO₂RR nor HER because they are not in direct contact with the substrate. Nevertheless, various recent studies have demonstrated that the M NPs encapsulated in carbon layers affect the other primary active sites around them, alter the adsorption/desorption strengths of the reaction intermediates, and generate new reaction pathways [26,27]. Several researchers have demonstrated that the Ni NPs embedded in N-doped carbon can enrich the electron density of the N-doped species and optimize the reaction energy barrier of the rate-determining step (COOH* formation) and CO desorption [27–30]. Most recent study shows that Ni NPs can trigger the electron donating effect and alter the charge density on the Ni–N₃ sites, thereby optimizing the binding strength of the key reaction intermediate COOH* on the Ni–N₃ sites [25]. Therefore, coupling of M NPs with M–N_x and N-doped sites in a suitable manner is an effective strategy for further uplifting the CO₂RR activity. When M NPs coexist with both M–N_x, N-doped sites, it is necessary to identify the origin of the catalytic activity and the mechanism of interactions of these M NPs with the M–N_x and N-doped sites at the interface. Moreover, the synergistic interaction of diverse components can disrupt the inherent adsorption energy scaling relation of reaction intermediates [31]. Despite their importance in the rational design of efficient electrocatalysts, it remains challenging to clarify the origin of the catalytic activity and the mechanism by which the synergistic effects enhance the reaction kinetics in CO₂RR.

Considering these aspects, this paper proposes a simple and scalable vacuum-assisted low temperature pyrolysis method to synthesize Ni-NP-encapsulated single-atomic Ni–N₄ sites dispersed on N-rich carbon nanotubes (Ni-NCNT). This low temperature strategy ensures the high density of identical Ni–N₄ sites and abundant uncoordinated N-doped species, thereby eliminating the intrinsic defects and low-coordinated Ni–N_x sites that function as active sites for CO₂RR [7,19]. The ratio of the N-doped species to the Ni–N₄ moieties in the carbon matrix can be tuned by controlling the composition of the reaction mixture, and thus, the electrochemical CO₂RR activity and selectivity can be optimized. Furthermore, the porous carbon nanotube (CNT) network structures with large surface areas provide highly accessible active sites that can help achieve a high electronic conductivity and fast electron transfer pathway [32–34]. Results of preliminary catalyst screening show that the CO₂RR activity is strongly related to the Brunauer–Emmett–Teller (BET) surface area and the sum of the uncoordinated pyridinic N and Ni–N₄ sites. To clarify the role of the Ni NPs, two acid treatments are applied to selectively remove the surface exposed Ni NPs and bulk Ni NPs enclosed in carbon layers. These treatments can alter the surface chemistries of the catalysts, clarify the previously unknown CO₂RR activity–property relationships, and provide new insights into the active catalyst structure. The Ni-NCNT catalysts treated with a mild acid promote CO₂ to CO conversion with a CO Faradaic efficiency (FE_{CO}) of 97.4% at a potential of −0.7 V vs. reversible hydrogen electrode (RHE) and a high CO partial current density (j_{CO}) of 58 mA cm^{−2} at a potential of −1.0 V in H-cell, superior to those of the existing Ni–N–C catalysts. Results of in-depth characterization and controlled electrochemical experiments show that the synergistic effect between the uncoordinated pyridinic N and Ni–N₄ sites improves the CO₂RR performance. Density functional theory (DFT) calculations demonstrate that (i) the uncoordinated pyridinic-N sites lower the energy barriers of the rate-limiting steps of COOH* formation on the Ni–N₄ sites; (ii) through strong

interactions, the Ni NPs chemically bond with Ni single atoms, thereby hindering the electron transfer for the COOH* formation with negligible influence on the electronic structures of the Ni–N₄ sites; (iii) the van der Waals interaction of Ni NPs increases the electron density of the uncoordinated N-doped species and optimizes the free energy barriers of COOH* formation, thereby promoting the reaction kinetics of CO₂RR catalysis. The findings highlight the key role of Ni NPs and N-doped species in modulating the electronic structure of the Ni–N₄ species to lower the absorption energy for the COOH* and CO* reaction intermediates and enhance the CO₂RR performance. The proposed synthesis method is a promising alternative to traditional high-temperature pyrolysis for single atom catalysts and can broaden the scope of the cooperative effects of different components. Furthermore, this research emphasizes that the electronic-structure-modulation-induced synergistic effects must not be disregarded while exploring this novel class of catalytic materials.

2. Materials and characterizations

2.1. Synthesis of Ni-NCNT catalysts

Melamine (10 g) (Sigma Aldrich) and different amounts of nickel (II) acetylacetone (Sigma Aldrich) were dispersed in 100 mL of ethanol (Daejung Chemicals, Korea). After stirring for 8 h at room temperature, ethanol evaporated using a rotavapor. The dried mixture was placed in a ceramic boat covered with a lid and transferred to a tube furnace with a high vacuum pump. Subsequently, the tube furnace was evacuated to $\sim 10^{-2}$ Torr and heated from room temperature to 500 °C at a heating rate of 5 °C min^{−1} for 2 h. Ar (200 sccm) was continually fed during the calcination while maintaining a partial pressure of $\sim 5 \times 10^{-1}$ Torr. After the mixture was cooled to room temperature, a black fluffy substance was obtained that was directly used for characterization and electrocatalytic CO₂ reduction evaluation. A series of Ni-NCNT catalysts were synthesized by varying amounts of nickel (II) acetylacetone and referred as Ni-NCNT-1 (0.125 mmol), Ni-NCNT-2 (0.25 mmol), Ni-NCNT-3 (0.5 mmol) and Ni-NCNT-4 (0.75 mmol).

2.2. Synthesis of Ni-C catalysts

The Ni-C catalyst was synthesized in a manner similar to the abovementioned method, except that glucose (5 g) (Sigma Aldrich) and 0.5 mmol of nickel(II) acetylacetone were used as the precursors.

2.3. Synthesis of N-CNTs

N-doped CNTs were synthesized using a mixture of 200 mg of commercial CNTs (Sigma Aldrich) and 10 g of melamine. The calcination procedure was similar to that in the synthesis of the Ni-NC catalysts. The inductively coupled plasma mass spectrometry (ICP-MS) analysis confirms the no metal species in the N-CNTs catalysts.

2.4. Synthesis of NiPc@CNT

First, carbon nanotubes (CNTs) were calcined at 500 °C in air for 5 h, followed by treatment with a 5 wt% HCl aqueous solution and sonication for 30 min. The purified CNTs were collected by filtration and thoroughly washed with deionized water. Next, 30 mg of the purified CNTs was dispersed in 30 mL of N,N-dimethylformamide (DMF) using sonication. Then, 10 mg of nickel phthalocyanine (NiPc) dissolved in DMF was added to the CNT suspension. The mixture was sonicated for 30 min to ensure a well-mixed suspension and then further stirred at room temperature for 20 h. Afterwards, the mixture was subjected to centrifugation, and the resulting precipitate was washed with DMF and ethanol before being dried at 80 °C under vacuum conditions. This process yielded the final NiPc@CNT material.

2.5. Characterization

X-ray powder diffraction (XRD) analysis was conducted on a Rigaku Ultima IV X-ray diffractometer with a Cu K α radiation ($\lambda = 1.5406 \text{ \AA}$) source operating at 40 kV and 200 mA. Raman spectra were obtained using a Horiba Jovin Yvon (LabRam Aramis) device at an excitation wavelength of 532 nm. The morphology was observed through field emission scanning electron microscopy (FE-SEM, JEOL-7800) and transmission electron microscopy (TEM; JEOL, F200). High-angle annular dark-field scanning transmission electron microscopy (HAADF-STEM) analysis was performed using a JEOL JEM-ARM 200CF instrument equipped with a spherical aberration corrector, operating at an accelerating voltage of 200 kV. X-ray photoelectron spectroscopy (XPS) measurements were obtained using a K-alpha system (Thermo UK) and Al K α (1486.6 eV) monochromatic X-rays. The XPS spectra were deconvoluted using the XPSpeak41 software, and the peak positions were corrected against the C 1 s peak (284.6 eV) originating from adventitious carbon. The Ni contents in the catalysts were quantified through inductively coupled plasma mass spectrometry (ICP-MS; OPTIMA-8300). Synchrotron-based X-ray absorption near-edge structure (XANES) and extended X-ray absorption fine structure (EXAFS) measurements were obtained at the Hard X-ray Micro-Analysis beamline at Pohang Light Source, Korea. The electron storage ring was maintained at 3.0 GeV with a variable beam current. A monochromatic beam was obtained using a double crystal Si (111) monochromator that was equipped with a second crystal for detuning the monochromatic X-ray beam to reduce its high harmonic components. Data was collected in the fluorescence mode by using a Ge detector at room temperature.

2.6. Electrochemical measurements

All electrochemical measurements were performed on a BioLogic VSP electrochemical workstation using a customized two-compartment gas-tight H-cell separated by a Nafion 117 membrane. The working electrode was prepared by dropping 50 μL of catalyst ink onto a carbon fiber paper (Toray TGP-H-60) with an active area of 0.25 cm^2 . The catalyst ink was prepared as follows: The synthesized catalysts (2 mg) were added to a solution of 970 μL ethanol and 30 μL Nafion solution (5 wt%), and this mixture was ultra-sonicated for 1 h to obtain a homogeneous catalyst ink. The counter electrode, reference electrode, and electrolyte were Pt, Ag/AgCl (saturated KCl), and 0.5 M KHCO₃, respectively. Before each experiment, the cathodic compartment of the H-cell was purged with CO₂ for 30 min, and the saturated 0.5 M KHCO₃ solution was measured to have a pH of 7.3. An LSV analysis was performed with a scan rate of 10 mV s⁻¹ from -0.63 V to -1.83 V vs. Ag/AgCl. All potentials measured against the reference electrode were converted to the reversible hydrogen electrode (RHE) scale using the following expressions: E (vs. RHE) = E (vs. Ag/AgCl) + 0.197 V + $0.0591 \times \text{pH}$. Catalytic performance tests were conducted in chronoamperometry conditions for 30 min. A gas chromatography (GC) instrument (YL instrument, Model 6500), equipped with a thermal conductivity detector and flame ionization detector, was used to quantify the gas phase products after 1800 s of bulk electrolysis. Electrochemical impedance spectroscopy (EIS) measurements were performed by applying an AC voltage with an amplitude of 5 mV in a frequency range of 100 kHz to 100 MHz.

The Faradaic efficiency of the gas products was calculated as

$$\text{FE} = \frac{Q_i}{Q_{\text{total}}} = \frac{N_i \cdot n \cdot F}{Q_{\text{total}}} \quad (1)$$

where,

Q_{total} : charge passed, C;

Q_i : charge used for the reduction of certain products, C;

N_i : number of moles for a specific product (measured by GC), mol;

n : number of electrons exchanged for product formation (= 2 for CO and H₂);

and F: Faradaic constant (= 96,485 C mol⁻¹).

The stability of the catalyst was tested at -0.6 V and -0.8 V (vs. RHE). The tested electrode was washed with deionized water and dried at room temperature overnight. Finally, the catalysts were removed from this electrode and dispersed in ethanol for XPS and HAADF-STEM measurements.

3. Results and discussion

3.1. Characterization

The Ni NPs encapsulated in N-doped carbon nanotubes with atomically dispersed Ni-N₄ species and abundant uncoordinated N-doped sites were synthesized at a low temperature (500 °C) and low-pressure condition by using a solid-state method, as shown in Fig. 1. Melamine and nickel acetylacetone mixed in different ratios were used as precursors. Under low pressure and temperature carbonization (400 °C to 600 °C), both melamine and nickel acetylacetone decomposed and attained a molten state. The reducing gases consisting of ammonia and hydrocarbons produced from melamine decomposition reduced Ni²⁺ ions into Ni nanocatalysts, which catalyzed the residual hydrocarbons to form N-doped carbon nanotubes (N-CNTs) [35,36]. Parallel to this reaction, a portion of the Ni²⁺ ions were coordinated with N by strong Lewis acid–base interactions to form atomically dispersed Ni-N₄. The carbon encapsulated Ni NPs were located at the tip of the CNTs, implying that CNTs grow via a vapor–liquid–solid (VLS) mechanism [37, 38]. It is noted that Ni-containing graphitic carbon nitride (Ni@C₃N₄) was observed only when the synthesis was conducted under atmospheric pressure, but at similar temperature conditions (Fig. S1). This suggests that the use of vacuum conditions is necessary to facilitate the direct growth of nitrogen-doped carbon from melamine, without the formation of intermediate C₃N₄ structures, at lower temperatures. Although the precise growth mechanism of N-CNTs under low temperature and pressure conditions is still not fully understood [39], prior research suggests that the vaporization temperature of melamine within the reaction zone plays a crucial role in governing their formation at lower temperatures and pressures [39,40]. However, it should be noted that the investigation of the complex compounds generated during the thermal decomposition process of melamine at lower temperatures falls outside the scope of this study. Under low-pressure conditions, it is believed that melamine undergoes spontaneous decomposition into hydrocarbons, even at temperatures lower than the typical decomposition temperature of melamine. This decomposition process results in the precipitation of N-doped carbon on the surface of nickel (Ni) [41]. Conversely, under high-pressure conditions, melamine tends to undergo rearrangement, forming tri-s-triazine units that further condense to form C₃N₄, even in the presence of Ni catalysts [42]. The synthesized N-CNT combined with the atomically isolated low-valent Ni (I) species to provide a large specific surface area and exposed active sites for efficient CO₂-to-CO reduction. The yield of the catalyst increased with the nickel content, and no catalysts were obtained when pure melamine was used as the precursor. This result indicated that the Ni metal functioned as a catalyst in growing the N-CNTs during the pyrolysis [38]. To the best of our knowledge, the synthesis of high-density single atom Ni-N₄ sites on N-CNTs has not been observed at temperatures as low as 400 °C [43–45]. However, herein, the catalysts synthesized at 500 °C were used for the characterization and catalytic studies.

SEM and TEM analyses were performed to investigate the morphology and microstructure of the prepared Ni-NCNT catalysts. The SEM images of Ni-NCNT (Fig. 2a, Fig. S2) indicated the presence of a combination of nanotube and nanosheet structures. Only short CNTs were found in the Ni-NCNT-1 sample (Fig. S2a), and the length and width of the CNTs increased from Ni-NCNT-2 to Ni-NCNT-4 (Fig. 2a, Fig. S2b, S2c). These observations indicated that increasing the Ni content favored the formation of longer and thicker CNT structures, attributable to the catalytic effect of Ni [35,36]. The TEM images

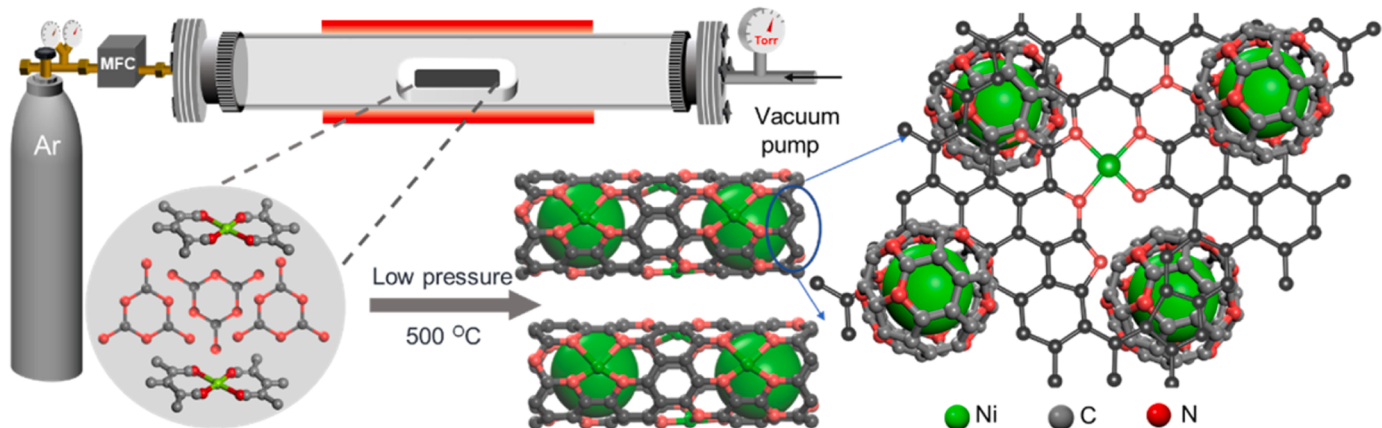


Fig. 1. Schematic of Ni-NP-encapsulated Ni-N-C nanotube catalysts.

confirmed the nanotube morphology in the Ni-NCNT samples, with the Ni NPs concentrated at the tip of the CNTs (Fig. 2b, Fig. S3a–S3c). These Ni nanoparticles were enclosed by highly graphitized carbon shell with 4–15 layers (Fig. 2c, Fig. S4). The thickness of carbon shell measured to be ~2–3 nm, ~3–5 nm, ~4–8 nm and ~10–12 nm for Ni-NCNT-1, Ni-NCNT-2, Ni-NCNT-3 and Ni-NCNT-4, respectively (Fig. S4). The Bragg diffraction theory was employed to determine the crystallite size of the Ni particles from the XRD pattern. The calculated average crystallite size is approximately 30 nm, which closely corresponds to the TEM data presented in Fig. 2. The lattice spacing of the Ni NPs was 0.209 nm, corresponding to the (111) crystal planes (Fig. S3d). Furthermore, the high-resolution TEM (HR-TEM) image revealed a highly crystalline multi-walled CNTs (Fig. 2d). Aberration-corrected high-angle annular dark-field scanning TEM (HAADF-STEM) imaging was performed to confirm the atomic distribution of isolated Ni atoms. The HAADF-STEM image of Ni-NCNT-3 samples revealed atomic Ni sites (Fig. 2e), indicating the presence of Ni–N₄ species across the carbon framework. A TEM-EDS line-scan analysis, performed along a linear path passing through the peripheral and central parts of a representative nanotube (Fig. 2f), showed that the Ni, N, and C contents increased toward the particle center. In other words, the Ni–N₄ sites were uniformly distributed across the nanotube structure. The scanning TEM (STEM) and energy dispersive X-ray analysis (STEM-EDX) elemental mapping images showed the overlay of N and Ni elements across the tubular structure of the carbon matrix for the Ni-NCNT-3 samples (Fig. 2g). The homogeneous distribution of Ni–N₄ sites on nanotube architecture with porous network offered abundant active sites and enabled efficient mass transport for CO₂RR. These results indicated that Ni encapsulated N-doped CNTs with atomically dispersed Ni–N₄ species were successfully synthesized at low temperatures.

The XRD patterns of all Ni-NCNT revealed two typical peaks at ~44.5° and ~51.9°, attributed to the (111) and (200) planes of Ni⁰, respectively (PDF #04–0850). This observation verified the existence of metallic Ni NPs (Fig. 3a) [12]. In addition, all samples showed two distinct peaks at ~21.2° (PDF #75–1621) and ~26.2° (PDF #75–1621) related to amorphous carbon (disordered) and graphitic carbon, respectively [12,46,47]. No XRD peaks related to graphitic carbon nitride (C₃N₄) were observed, confirming that melamine was directly transformed to carbon rather than C₃N₄ [48]. The amorphous nature of carbon indicated a highly disordered structure. Raman spectroscopy was performed to determine the graphitization degree and surface defects of the catalysts (Fig. 3b). All Ni-NCNT catalysts exhibited two peaks at 1355 cm⁻¹ (D band) and 1585 cm⁻¹ (G band), attributable to the defects and bond stretching of the sp² carbon, respectively [32,46]. The ratios of the intensity of D-and G-Raman peaks (I_D/I_G) for Ni-NCNT-1, Ni-NCNT-2, Ni-NCNT-3, and Ni-NCNT-4 were calculated to be 1.09, 1.04, 1.04, and 1.05, respectively, indicating that in all Ni-NCNT

catalysts, the graphitized carbon and defects were in a balanced and appropriate state. These findings highlighted that the Ni NPs improved the graphitization degree, whereas the Ni single atoms and N-dopants induced the defect states in the carbon lattice [45]. Additionally, the peak at 2700 cm⁻¹ (2D band) demonstrated the satisfactory degree of graphitization, and the broad width of the 2D band indicated the presence of multilayer graphene [49]. The high degree of graphitization was expected to increase the electron transfer rate, and the defect states were expected to promote the CO₂RR.

The chemical valence state and surface element composition of the Ni-NCNT catalysts were investigated using XPS. The survey spectra confirmed the presence of C, N, O, and Ni components in all Ni-NC catalysts (Fig. S5). The high-resolution C 1 s spectrum was deconvoluted into four peaks attributable to C–C (284.6 eV), C–N (285.2 eV), C–O (287.1 eV), and C=O (289.4 eV) (Fig. S6) [46,50]. The high-resolution N 1 s spectra revealed the presence of porphyrin-like Ni–N moieties at binding energies of ~399.2 eV and pyridinic N (~398.2 eV), pyrrolic N (~400.9), graphitic N (~401.5 eV), and oxidized N (~404.6 eV) species (Fig. 3c) [7,32,51,52]. The N content (%) estimated from the elemental analyses (EA) and XPS exhibited the following trend: Ni-NCNT-4 (12.6 and 15.63) > Ni-NCNT-3 (11.51 and 12.08) > Ni-NCNT-2 (8.62 and 11.84) > Ni-NCNT-1 (6.05 and 10.06). In other words, the N content in Ni-NCNT-4 was higher than that in the other three samples. The difference in the N contents determined by the EA and XPS analysis suggested that the doped N in the all the Ni-NCNT catalysts was predominantly present on the surface and edges rather than in the bulk. Table S1 and Fig. 3d summarize the proportions and overall N contents of all Ni-NCNT samples. As shown in Fig. 3d, the porphyrin-like Ni–N moieties were dominant in all Ni-NCNT samples, accounting for 45% of the total N content, whereas Ni-NCNT-3 had the highest Ni–N moieties (49.7%) among all samples. In general, higher Ni–N moieties have been proven to be the primary active sites for CO₂RR, and thus, they were expected to enhance the CO₂RR performance [7,53]. Furthermore, the N-doping content quantified by the XPS was considerably higher than the Ni content quantified by XPS for Ni-NCNT-1 (3.4 at%), Ni-NCNT-2 (3.6 at%), Ni-NCNT-3 (3.8 at%), and Ni-NCNT-4 (3.7 at%), demonstrating that abundant N-dopants that were not coordinated with the Ni atom co-existed in the all Ni-NCNT samples. The high-resolution Ni 2p spectra of Ni-NCNT catalysts showed two minor peaks at ~853.2 eV and ~856.7 eV, attributable to metallic Ni⁰ and oxidative Ni²⁺, respectively (Fig. 3e). The other high-intensity peak found at ~854.8 eV corresponded to the low-valent Ni (I) bound to N, and the results are consistent with those of HAADF-STEM, confirming the existence of Ni–N₄ species. The Ni atomic contents in the Ni-NCNT samples measured from the XPS and ICP-MS were different (Table S2), attributable to the bulk Ni concentration owing to the encapsulation of multi-layered carbon shells. The bulk Ni content declined from

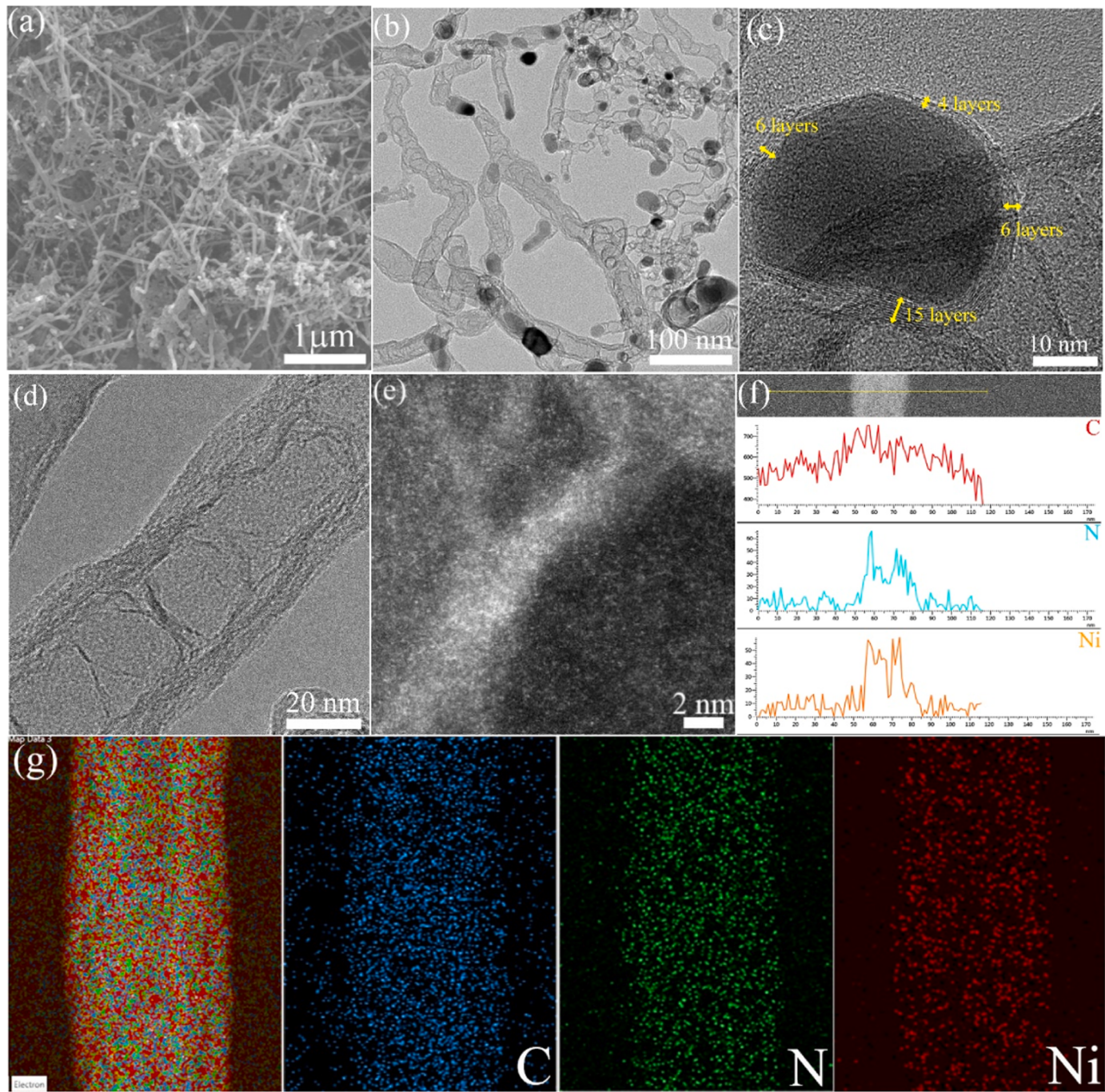


Fig. 2. Structural characterization: (a) SEM image of Ni-NCNT-3, (b) TEM image of Ni-NCNT – 3, (c) HR-TEM image of Ni-NCNT-3 showing N-doped carbon encapsulated Ni NPs, (d) HR-TEM image of CNT in Ni-NCNT-3, (e) HAADF-STEM image of Ni-NCNT-3, (f) TEM-EDX line-scan on CNT, and (g) EDS mapping (Ni, N, and C) of CNT in Ni-NCNT-3 catalysts.

Ni-NCNT-1 to Ni-NCNT-4, whereas the bulk N-doped content significantly increased. These findings indicated that increasing the Ni content in the reaction mixture increased the CNT precipitation owing to the catalytic effect of Ni NPs. As a result, this phenomenon leads to an increase in the thickness of the carbon shell and a decrease in the Ni bulk content by elevating the density of Ni–N₄ sites throughout the CNT structure [12]. However, the XPS analysis results highlighted that the Ni-NCNT-3 catalyst contained considerably higher amounts of Ni–N₄ species than the other catalysts, while the surface of the Ni-NCNT-4 catalyst contains substantial quantities of uncoordinated N-doped species (Tables S1 and S2). This can be attributed to a fraction of the atomically dispersed Ni becoming integrated into the bulk carbon layers,

rather than remaining exclusively on the surface layer of the carbon. Furthermore, the specific surface areas of Ni-NCNT-1, Ni-NCNT-2, Ni-NCNT-3, and Ni-NCNT-4 were calculated to be 112, 113, 221, and 149 m² g⁻¹ by using the BET model (Fig. S7 and Table S3). Specifically, the surface area increased with increasing Ni content in the catalysts and then decreased in Ni-NCNT-4.

Electron paramagnetic resonance (EPR) spectroscopy was performed to identify the unpaired electrons in monovalent Ni(I) (Fig. S8). The g value (2.36 to 2.42) of Ni-NCNT in the EPR spectrum was assigned to the unpaired electron in Ni(I) 3d_{x²-y²} orbital [34]. The EPR spectrum intensity for Ni-NCNT-1 was higher than that for the other Ni-NCNT samples owing to the high electron density caused by the presence of

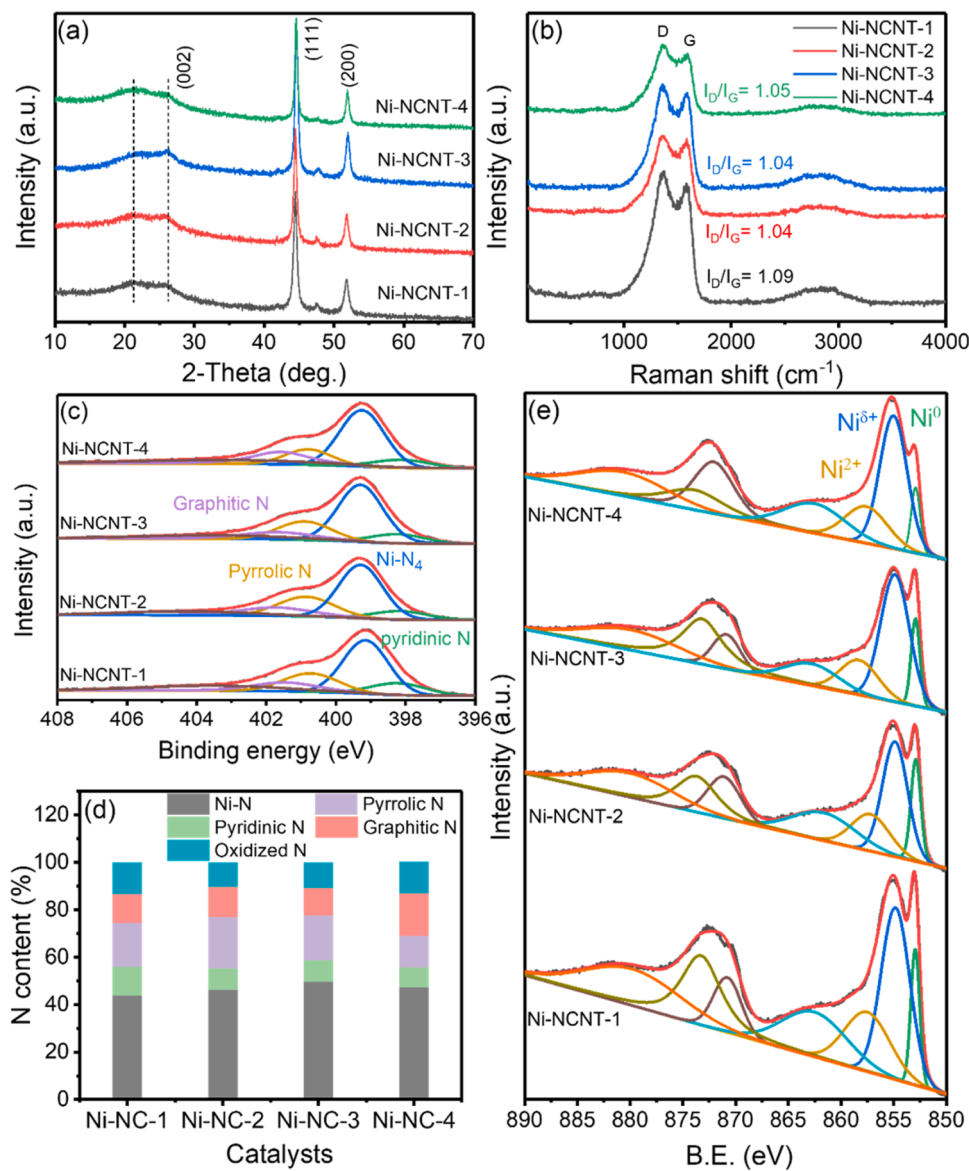


Fig. 3. (a) XRD spectra, (b) Raman spectra, (c) deconvoluted N 1 s XPS spectra, (d) contents of Ni–N₄, pyridinic N, pyrrolic N, graphitic N, and oxidized N derived from N 1 s XPS spectra, and (e) Ni 2p XPS spectra of various Ni-NCNT catalysts.

Ni NPs [25]. Overall, the characterization results supported the effective synthesis of N-doped CNT confined Ni NPs consisting of monovalent Ni single atoms and numerous uncoordinated N-doped sites.

3.2. Electrocatalytic CO₂RR Performance of Ni-NCNT Catalysts

Owing to the single atomic Ni–N₄ sites and abundant N-doped species in porous carbon frameworks, the Ni-NCNT samples are promising CO₂RR electrocatalysts. The CO₂RR activity of Ni-NCNT electrocatalysts was measured through linear sweep voltammetry (LSV) in a gas tight H-type cell with the two compartments separated by a Nafion-117 proton exchange membrane. Compared with other Ni-NCNT catalysts, Ni-NCNT-3 had a substantially greater current density in the same potential region, implying a higher CO₂ electroreduction rate than those of the other three samples (Fig. 4a). Bulk electrolysis was performed at different potentials for 30 min to evaluate the reduction products. Gas chromatography (GC) revealed CO and H₂ as the reduction products, and no liquid products were detected with ¹H nuclear magnetic resonance spectra (not shown in the manuscript). For all catalysts and at all potentials, the total Faradaic efficiency (FE) of gaseous CO and H₂ was

approximately 100%, suggesting the exclusive production of CO and H₂. Fig. 4b compares the FE of CO (FE_{CO}) for various Ni-NCNT catalysts. Ni-NCNT-3 exhibited the best CO₂RR activity with FE_{CO} of 92% at -0.7 V vs. RHE (Fig. 4b). In addition, the Ni-NCNT-3 (131 mV dec⁻¹) catalysts presented the lowest Tafel slope (Fig. S9), with the corresponding values for Ni-NCNT-1, Ni-NCNT-2, and Ni-NCNT-4 being 146 mV dec⁻¹, 139 mV dec⁻¹, and 161 mV dec⁻¹, respectively. The value for Ni-NCNT-3 was close to the theoretical value of 118 mV dec⁻¹, suggesting that the first electron transfer for the COOH* species was the rate-determining step for the overall process [7,27]. Furthermore, the number of exposed active centers for CO₂RR catalysis in Ni-NCNT-3 was higher than those in the other three Ni-NCNT catalysts. This finding was supported by the larger electrochemical surface active area (ECSA) of Ni-NCNT-3 (238 cm²) compared with those of Ni-NCNT-1(186 cm²), Ni-NCNT-2 (196 cm²), and Ni-NCNT-4 (150 cm²) catalysts, determined using the electrochemical double-layer capacitance (C_{dl}) method (Fig. 4c, Fig. S10). The higher ECSA of Ni-NCNT-3 was attributable to the large number of exposed active sites associated with the large surface area, as determined from the BET results. Therefore, the high CO₂RR selectivity and activity of Ni-NCNT-3 were strongly correlated

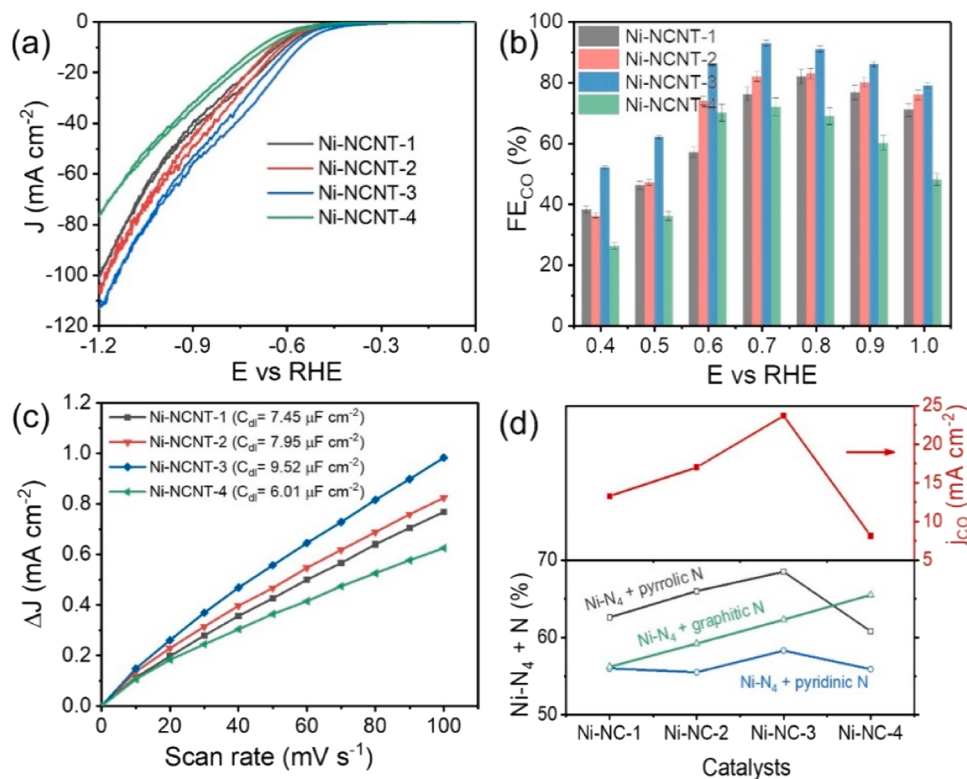


Fig. 4. Comparison of the activity and selectivity of Ni-NCNT electrocatalysts. (a) LSV curves of Ni-NCNT catalysts in CO_2 -saturated 0.5 M KHCO_3 electrolytes, (b) Faradaic efficiency of CO (FE_{CO}), (c) difference in the capacitive current density plotted against the scan rates of various Ni-NCNT catalysts, and (d) comparison of the j_{CO} of different Ni-NCNT catalysts with the corresponding summation of Ni-N_4 and different atomic N contents.

with the Ni-N_4 species and high BET surface area. Despite Ni-NCNT-4 having a larger number of Ni-N_4 sites and demonstrating a higher BET surface area in comparison to Ni-NCNT-1 and Ni-NCNT-2, its CO_2RR activity is lower. This lower activity in Ni-NCNT-4 can be attributed to its reduced ECSA in comparison to Ni-NCNT-1 and Ni-NCNT-2. This observation suggested that in addition to the Ni-N_4 and BET surface area, other factors influenced the CO_2RR activity of Ni-NCNT catalysts. In other words, the superior CO_2RR performance of Ni-NCNT-3 was not entirely associated with the number of exposed active Ni-N_4 sites and may also be related to N-doped atoms and Ni NPs. It could also be hypothesized that the difference in N-moieties in the Ni-NCNTs led to the differences in the catalytic activity [15,54]. The higher CO_2 reduction activity of Ni-NCNT-3 was also confirmed by the electrochemical impedance spectroscopy (EIS) results. In the Nyquist plot, the semicircle diameter for Ni-NCNT-3 was smaller than those of the other Ni-NCNT catalysts, as shown in Fig. S11. This result demonstrated the low interfacial charge-transfer resistance of Ni-NCNT-3, which facilitated the kinetics of CO_2 reduction.

To further evaluate the factors influencing the CO_2RR activity of Ni-NCNT catalysts, the dependence of the intrinsic CO_2RR activity on the N dopant contents in Ni-NCNT was studied [15,21,55]. The CO_2RR performance of Ni-NCNT revealed that the trend of the j_{CO} of the Ni-NCNT catalysts was similar to that of the sum of $\text{Ni-N}_4 + \text{pyridinic N}$ and $\text{Ni-N}_4 + \text{pyrrolic N}$ contents but not correlated with the $\text{Ni-N}_4 + \text{graphitic N}$ (Fig. 4d). This observation suggested that the pyridinic and pyrrolic N species in the Ni-NCNT were active for CO_2RR , consistent with previously reported results [55]. In other words, the optimized percentage of uncoordinated N-doped species in the Ni-NCNT helped enhance the CO_2RR activity. To validate if the pyridinic N and pyrrolic N sites were active sites for CO_2RR , a control experiment was performed in the presence of H_3PO_4 , which has been shown to block the pyridinic-N and pyrrolic-N sites in catalysts [56,57]. As shown in Fig. S12, the catalytic performance of Ni-NCNT-3 after PO_4^{3-} poisoning was considerably lower

than that of the fresh catalyst, which demonstrated that both the pyridinic-N and pyrrolic-N sites contributed to the CO_2RR .

To clarify the individual roles of Ni-N_4 and N-doped species in Ni-NCNT catalysts on the CO_2RR activity, control samples Ni-C (without Ni-N_4 species) and N-doped CNTs without Ni (N-CNTs) were synthesized (details are presented in the experimental section). The control Ni-C sample exhibited higher HER activity compared with that for CO_2RR (Fig. S13a, S13b), which demonstrated the key role of the Ni-N_4 species in achieving high FE_{CO} . The other control metal-free N-CNTs exhibited low FE_{CO} but high FE_{H_2} (Fig. S13b), which highlighted that the N-doped sites did not provide active sites for CO_2RR . Overall, neither the Ni nor N constituents alone promoted the CO_2RR . Instead, the formation of single atomic Ni-N_x sites contributed to the overall CO_2RR activity, as reported previously [12,27,58].

To gain deeper insights into the origin of the synergistic catalytic activity between Ni-N_4 sites and uncoordinated N-doped sites, a phenomenon that has not been explored in the context of CO_2RR performance, the performance of nickel (II) phthalocyanine immobilized on a CNT substrate (NiPc@CNT) was examined under similar conditions. This NiPc@CNT catalyst served as a heterogeneous catalytic platform, featuring well-defined Ni-N_4 active species and uncoordinated N-doped species (Fig. S14) similar to Ni-NCNT catalysts, enabling the unravelling of the structure-activity relationship in Ni-NCNT electrocatalysis for CO_2RR . A STEM-EDX elemental mapping images of NiPc@CNTs illustrates the even distribution of NiPc on CNTs (Fig. S15), and ICP-MS analysis reveals that NiPc@CNTs contain 1.6% of Ni atoms. The Ni 2p XPS spectra (Fig. S16a) and the N 1s spectra confirm the Ni-N_4 sites and uncoordinated N-doped sites (Fig. S16b), respectively. The electrocatalytic performance of NiPc@CNT catalysts exhibited a maximum FE_{CO} of 69% at a potential of -0.7 V vs. RHE (Fig. S17). Additionally, it was observed that the CO_2RR performance of NiPc@CNT significantly deteriorated upon the addition of a KSCN , attributed to the blockage of Ni sites by SCN^- ions (Fig. S17). To further investigate the possibility of

uncoordinated-N doped species as active sites in NiPc@CNT, PO_4^{3-} anions poison test was employed to selectively block the N-doped sites. This poisoning treatment resulted in comparable CO₂RR performance, indicating that the influence of uncoordinated N-doped species on CO₂RR performance is negligible on NiPc@CNT catalysts (Fig. S18). These findings explicitly confirm that Ni single atoms serve as the exclusive active sites for electrochemical CO₂RR in NiPc@CNT and no significant synergistic effect could be expected from the N-doped sites in this specific catalyst system. These results contrast with findings related to Ni-NCNTs catalysts, where Ni-N₄ and N-doped sites work together synergistically to boost the activity and selectivity of CO₂RR. This difference can be attributed to the presence of diverse components within Ni-NCNT catalysts, which introduce variations in the physico-chemical properties and regulate the electronic structure of the resulting Ni-NCNT materials. Indeed, previous reports confirm that the presence of additional N atoms within the M-N-C matrix has a notable impact on the activity of the M-Nx sites [59]. Additionally, a recent study has suggested that N-doping in the carbon shell of Ni NPs plays a substantial role in improving the adsorption and activation of CO₂ [27]. Hence, the presence of Ni NPs in Ni-NCNT catalysts might activate the N-doped sites during the CO₂RR.

Furthermore, the influence of encapsulated Ni NPs on the CO₂RR activity and selectivity was then investigated by acid leaching of the optimized Ni-NCNT-3 catalyst. Two acid leaching experiments were performed: in 0.5 M H₂SO₄ for 6 h at 60 °C to remove only the surface-exposed Ni NPs, and in 5 M HNO₃ for 12 h at 80 °C to remove the bulk Ni NPs, followed by calcination under an Ar atmosphere at 500 °C to remove the oxygen functional groups generated during the acid treatment. The resulting samples were designated as Ni-NCNT-3HS and Ni-NCNT-3HN. In the XRD graphs, the Ni⁰ peak was visible for the Ni-NCNT-3HS catalyst but nearly vanished for Ni-NCNT-3HN (Fig. S19a). These findings were consistent with the results of the ICP-MS analysis, as the Ni content significantly decreased from 57.1 wt% to 51.3 wt% and 5.7 wt% for the Ni-NCNT-3HS and Ni-NCNT-3HN catalysts after acid leaching, respectively (Table S2). In addition, the peak at ~21.2° disappeared completely, and other peak at 26.2° became dominant owing to the removal of disordered graphitic carbon during the acid treatment [47,60]. The Raman spectra indicated the increase in the ratio of the G to D band after acid washing, with the increase being more notable for the Ni-NCNT-3HN sample (Fig. S19b). This finding also suggested the removal of disordered graphitic carbon during washing [60].

The Ni 2p XPS spectra of both Ni-NCNT-3HS and Ni-NCNT-3HN exhibited a high intense peak corresponding to monovalent Ni(I) at ~854.6 eV, similar to the control sample. However, no distinctive signal was observed for metallic Ni⁰, which indicated that single Ni atoms were predominant on the catalyst surface (Fig. S20a, S20b), and the Ni particles in the Ni-NCNT-3HS were enclosed in a thick carbon layer. The high-resolution N 1 s XPS spectra (Fig. S20c, S20d) revealed the presence of Ni-N₄ and N-doped species in both samples. However, the overall N content and Ni-N₄ species slightly decreased in Ni-NCNT-3HS (Table S1), with the decline being more predominant in Ni-NCNT-3HN. These findings were reasonable given that the unstable N-dopants and surface exposed Ni species predominant on the surface were washed off during acid treatment. The Ni NPs encapsulated by multiple carbon layers could not be removed unless the carbon layers covering the Ni NPs were damaged [61]. In other words, strong acid washing could damage the carbon matrix, thereby affecting the catalytic properties.

The TEM analysis of Ni-NCNT-3HS indicated the presence of CNT encapsulated Ni NPs (Fig. S21a), whereas no Ni NPs were observed in the TEM image for Ni-NCNT-3HN (Fig. S21b). The HAADF-STEM imaging confirmed the presence of Ni single atoms in both catalysts (Fig. S21c, S21d). The results of the XRD, XPS, and TEM analysis highlighted that mild acid treatment removed the surface exposed Ni NPs and unstable N-species, while the carbon shell encased Ni NPs and Ni-N sites remained in the sample. Conversely, strong acid leaching not only removed the Ni NPs shielded by multilayer carbon but also damaged the

carbon structure, leading to the partial removal of Ni-N₄ sites and N-doped species. Consequently, only single Ni atoms remained in the Ni-NCNT-3HN catalysts, with no Ni NPs presence in the sample.

XANES and EXAFS spectroscopies were performed to explore the coordination environment and electronic structure of the Ni-NCNT catalysts. The XANES spectra (Fig. 5a) for both Ni-NCNT-3HS and Ni-NCNT-3HN highlighted a pre-edge line between that of Ni(II) phthalocyanine (NiPc) and Ni foil, indicating that the average valence of Ni atoms in the Ni-NCNT-3HS and Ni-NCNT-3HN was between Ni(0) and Ni(II). The phase uncorrected Fourier-transformed k²-weighted EXAFS spectra of Ni-NCNT-3HS and Ni-NCNT-3HN indicated a characteristic peak of the Ni-N bond at 1.4 Å and Ni-Ni bond at approximately 2.2 Å (Fig. 5b), comparable to those of the reference NiPc and Ni foil, respectively [26].

Subsequently, the CO₂RR performance of the acid-treated samples was assessed to verify the structure–activity relationship. The Ni-NCNT-3HS catalysts exhibited a higher FE_{CO} over the entire potential range compared with that of Ni-NCNT-3 (Fig. 5c). The maximum value was 97.4% at potential of -0.7 V vs. RHE, and the j_{CO} was 58 mA cm⁻² at -1 V (Fig. 5d). Notably, the CO₂RR process catalyzed by Ni-NCNT-3HS demonstrated high FE_{CO} with exceptional j_{CO}, outperforming most of the existing Ni-N-C catalysts in an H-cell setup (Table S4). The enhanced CO₂RR activity was attributed to the removal of surface exposed Ni NPs that were predominately active for the competing HER. Thiocyanate (SCN⁻) poisoning experiments revealed that the current density (Fig. S22a) and FE_{CO} of Ni-NCNT-3HS remained unchanged. In other words, the other active sites participated in the CO₂RR when the Ni-N₄ sites were blocked by the SCN⁻ ions, consistent with the active participation of the N-doped species in CO₂RR [18,19]. Notably, the Ni NPs enclosed in the thick carbon layer were not in direct contact with the surface reactants and thus did not have catalytic effect [12]. In contrast, the Ni-NCNT-3HN catalyst exhibited a low FE_{CO} of 82% at a potential of -0.7 V vs. RHE and a j_{CO} of -47.2 mA cm⁻² at -1.0 V vs. RHE, lower than those of the Ni-NCNT-3HS and Ni-NCNT-3 catalysts (Fig. 5d). The current density and FE_{CO} of Ni-NCNT-3HN further decreased in the presence of SCN⁻ (Fig. S22b), which indicated that the Ni-N₄ sites were the sole active sites for CO₂RR. The decrease in the CO₂RR activity was attributable to the leaching of bulk Ni NPs, single Ni atoms, and N-doped sites from the sample, as confirmed by the characterization (Fig. S19–S21). The other possible reason for the low CO₂RR of Ni-NCNT-3HN was carbon structure damage during the strong acid leaching, which reduced the number of active Ni-N species (Fig. S20) and increased the sample resistance (Fig. S23). The experimental results highlighted the synergistic roles of Ni-N₄ and N-doped sites in achieving a high electrocatalytic CO₂RR performance. However, the true function of Ni NPs was not clarified. Notably, the existing studies have highlighted that the Ni NPs alter the electronic structure of N-doped species and Ni-N₄ sites without directly involving the CO₂RR and boost the activity of CO₂RR [26,27]. Therefore, DFT calculations were performed to theoretically interpret the individual electrochemical activity of the Ni-N₄ and N-doped sites and the effect of Ni NPs on the amounts of Ni-N₄ and N-doped species in the context of the CO₂RR.

In addition to the high activity and selectivity, the long-term durability must be considered when evaluating the catalyst potential. As shown in Fig. S24, Ni-NCNT-3 maintains more than 85% FE_{CO} at a potential of -0.7 V vs. RHE, but the current density decreased over the electrocatalysis duration. This phenomenon likely occurred because the exposed Ni NPs and amorphous reduced the sample stability [12]. In contrast, Ni-NCNT-3HS and Ni-NCNT-HN were reasonably stable and exhibited an acceptable FE_{CO} after 24 h of continuous electrolysis (Fig. 5e). The architecture (Fig. S25) and chemical states of Ni and N (Fig. S26) remained nearly unchanged after long-term CO₂ reduction, indicating that excellent stability of the frameworks in long-term application.

To further emphasize the industrial importance of the Ni-NCNT-3HS catalysts, the stability of Ni-NCNT-3HS catalysts was assessed by

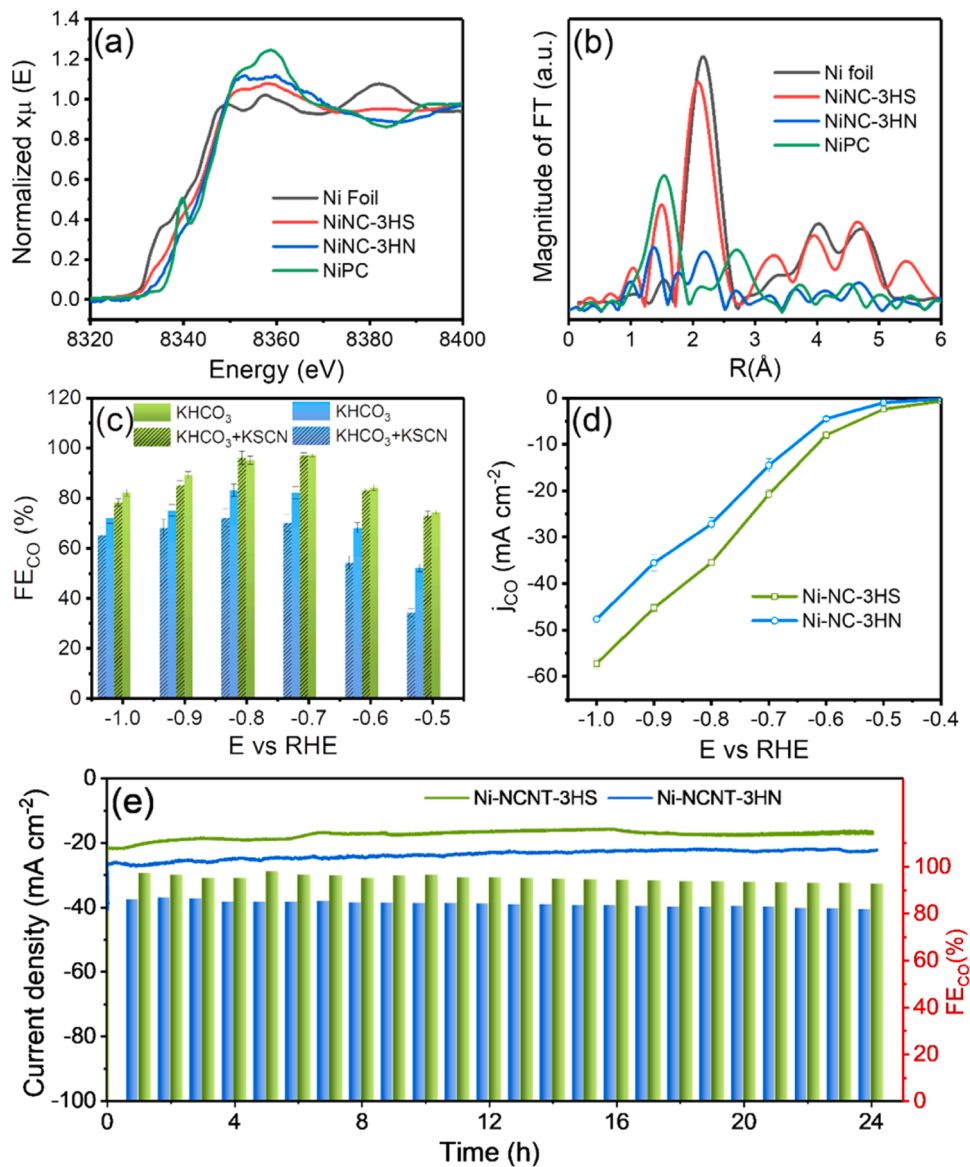


Fig. 5. (a) Normalized Ni K-edge XANES spectra, (b) EXAFS spectra of Ni-NCNT-3HS and Ni-NCNT-3HN with reference samples of Ni foil and NiPC, (c) FE_{CO} of Ni-NCNT-3HS and Ni-NCNT-3HN in KHCO₃ and KHCO₃ + KSCN solutions, (d) corresponding j_{CO} of these catalysts, and (e) chronoamperometric curve at an operation potential of -0.7 V vs. RHE for 24 h and Faradaic efficiencies in the stability tests for Ni-NCNT-3HS and Ni-NCNT-3HN samples.

fabricating gas diffusion electrode (GDE) based zero gap membrane electrode assembly (MEA) electrolysis system that used an anionic membrane. The fabrication process is detailed in the [Supporting Information](#) and Fig. S27 in the [supporting information](#) showed the digital graph of MEA electrode used in this study. As showed in Fig. S28 in the [supporting information](#), the MEA cell shows constant cell voltage of 2.65 V at an applied current density of 250 mA cm^{-2} for 200 h of continuous electrolysis. The MEA electrolysis results underscore the remarkable stability of Ni-NCNT-3HS, hinting at the possible utilization of Ni-NCNT catalysts in the context of commercial-scale electrolysis.

For the DFT studies, a series of structural models including bare isolated Ni-N₄ sites (Fig. S29a) and optimized Ni-N₄ sites embedded in various N-doped sites (Fig. 6a) were constructed to verify the synergistic interaction of Ni-N₄ sites and N-doped species. The models were expressed as Ni-N₄-X, where X (Ni, N1, N2, N3, N4, graphitic N (GH), pyridinic N (PD) and pyrrolic N (PY)) represent different candidate-active sites. According to previous reports, CO₂ electroreduction to CO involves two proton-coupled electron transfer steps to obtain COOH* and CO* intermediates [5,62]. The free energy diagrams shown

in Fig. S29b indicated that the Ni-N₄-Ni ($\Delta G_{\text{COOH}^*} = 1.065 \text{ eV}$) and Ni-N₄-N sites ($\Delta G_{\text{COOH}^*} = 1.974 \text{ eV}$) exhibited a large energy barrier for COOH* formation, which is considered the rate-determining step [63]. When the uncoordinated N-doped species were coupled with the isolated Ni-N₄ sites (Fig. 6b), the limiting barrier was reduced on both the Ni-N₄-Ni ($\Delta G_{\text{COOH}^*} = 0.618 \text{ eV}$) and Ni-N₄-N sites (Table S5). Similarly, CO* desorption on both sites was facilitated by the introduction of the uncoordinated N-doped sites except on the Ni-N₄-N site (Fig. S30). This result indicated that the uncoordinated N-doped sites could effectively alter the energy barrier on the Ni-N₄ sites. This observation explained the high FE_{CO} and j_{CO} for Ni-NCNT-3HS (Fig. 6b) [18,64]. Among the uncoordinated N sites, the Ni-N₄-PY site showed the lowest free energy change for COOH* formation ($\Delta G_{\text{COOH}^*} = 0.121 \text{ eV}$) but a large energy barrier for the CO* desorption (-1.989 eV), which limited CO desorption. The smaller energy barriers for COOH* (0.051 eV) formation and CO* (0.426 eV) desorption on Ni-N₄-PD compared to those for the Ni-N₄-N sites supported the experimental findings that pyridinic N synergistically contributed to the CO₂RR [64,65]. Furthermore, the DFT results were consistent with those of the ambient-pressure XPS analysis, which

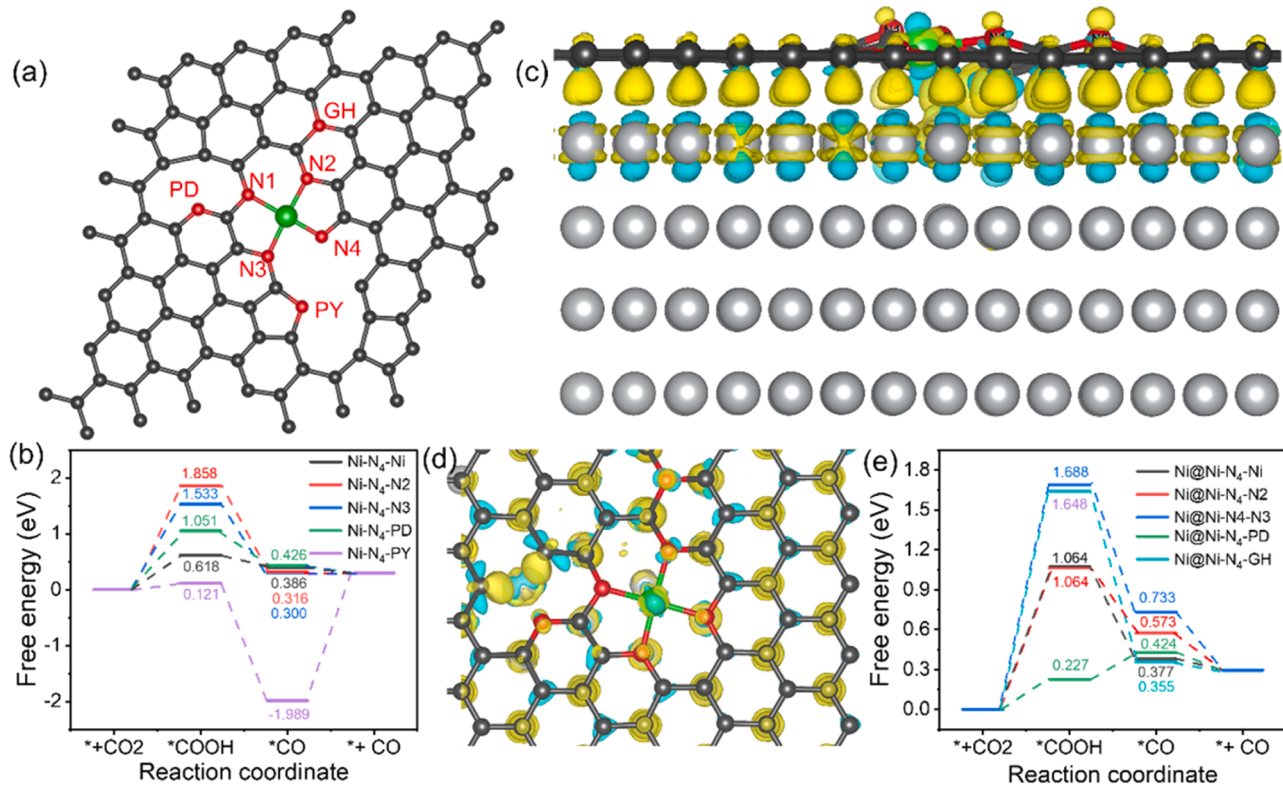


Fig. 6. DFT studies: (a) atomic structure of Ni-N₄ embedded uncoordinated N-doped species, (b) free energy diagrams for CO₂RR on various active sites, (c) side views of the charge density difference in Ni@Ni-N₄-X system. Yellow and cyan indicate charge accumulation and charge depletion, respectively, (d) charge density associated with the structural evolution of CO₂RR for optimized Ni@Ni-N₄-N (Ni NPs (light gray), Ni single atom (green), N (Red)), and (e) free energy profiles for the various optimized models during the CO₂RR.

demonstrated that the pyridinic-N sites not only functioned as preferential adsorption sites for CO₂ and active sites for CO₂RR, but also increased the binding strength of COOH* intermediate on the Ni-N₄ sites [66]. In contrast, for Ni-N₄-GH, the COOH* intermediate was not absorbed onto the graphitic N site, and thus, the catalytic activity of Ni-N₄-GH site was negligible (Fig. S31). This observation could be explained by the fact that the electrons in graphitic N were located in the antibonding π^* orbital and were thus not accessible for CO₂ binding [15,67]. Additionally, the adsorption free energy of hydrogen (ΔG_{H^*}) was calculated on each site to evaluate the HER electrocatalytic activity [34]. The ΔG_{H^*} values were +1.295 eV (Ni-N₄-Ni), +1.241 eV (Ni-N₄-N1), +1.688 eV (Ni-N₄-N2), +1.168 (Ni-N₄-N3), and -1.374 eV (Ni-N₄-N4), far from the optimal ΔG_{H^*} (0 eV) for HER, indicating well suppressed HER on all sites (Fig. S32a). Nevertheless, the HER process on Ni-N₄-PD required an overpotential of 0.174 eV, showing that the HER process was slightly favored on the Ni-N₄-PD active site compared with the other sites. The Ni-N₄-PD site was easily poisoned by the H* intermediate that blocked the CO₂RR kinetics. Overall, the additional uncoordinated N-dopants optimized the electronic structures of the Ni-N₄ centers, thereby improving the reaction kinetics of CO₂ adsorption and CO desorption, resulting in enhanced CO₂RR catalysis.

Furthermore, DFT studies were performed to investigate the role of Ni NPs on the CO₂RR activity of the Ni-N₄ and uncoordinated N-doped sites. Given that the direct growth of N-doped graphene on Ni caused a small separation between them (0.21 nm) [68], Ni-N₄ sites embedded in various N-doped sites were constructed around the Ni(111) particle, which was used as the targeted structure for DFT studies (Fig. 6c). The structure of Ni-N₄ was affected by the Ni NPs when pyrrolic N was introduced close to Ni-N₄ (Fig. S33). This phenomenon changed the geometric structure of Ni-N₄ and destabilized the structure. Therefore, pyrrolic N sites were not considered in the DFT calculations. A modified

structure without pyrrolic N sites was constructed, and the active sites were designated as Ni@Ni-N₄-Ni, Ni@Ni-N₄-N2, Ni@Ni-N₄-N3 Ni@Ni-N₄-PD, and Ni@Ni-N₄-GH (Fig. 6c). As shown in Fig. 6c, the first layer of Ni(111) easily banded with the N-doped carbon structure and Ni-N₄ sites, resulting in enhanced electron transfer from Ni(111) to the carbon layer [25,27]. Bader charge analysis confirmed increased electron density (5.1 e) on the carbon layer, whereas the top layer of Ni exhibited decreased electron density with an atomic Bader charge of 4.6 e. The charge density difference plots differentiated the electron accumulation (yellow) and electron depletion (cyan) on several C- and N-atoms, depending on the proximity of the Ni particle to the atoms (Fig. 6d) [25]. The increased electron density enhanced the adsorption of reaction intermediates and desorption of CO. As shown in Fig. 6e, the absorption energy of COOH* formation on Ni@Ni-N₄-Ni (1.064 eV) and Ni@Ni-N₄-N3 (1.688 eV) sites was lower than that of the corresponding Ni-N₄-Ni and Ni-N₄-N3 sites, whereas the binding strength improved over the Ni@Ni-N₄-N2 (1.064 eV) sites. The distinct CO₂RR activity was attributable to the charge redistribution between the Ni NPs and the anchoring site [69]. For example, the charge density plots highlighted the occurrence of charge sharing between the Ni NPs and Ni atoms of Ni-N₄, and the N3 and N4 atoms in the carbon layers bonded chemically, which prevented electron transfer, promoted CO₂ adsorption, and rendered the production of COOH* on these sites thermodynamically challenging [69,70]. Consequently, the COOH* formation energy of the Ni site of Ni@Ni-N₄-X was comparable to that of the Ni of the bare Ni-N₄ sites (Fig. S29), suggesting that the Ni NPs do not affect the catalytic characteristics of Ni atomic sites even in the presence of N-doped sites. Moreover, both pyridinic N and graphitic N were not in proximity of the Ni NPs and were connected only by van der Waals interaction. The enhanced electron-donating ability facilitated the *CO₂ hydrogenation to *COOH formation [71]. Consequently, the free energies of COOH* intermediate formation on the Ni@Ni-N₄-PD (0.227 eV) were

lower than those of the corresponding Ni–N₄-PD (1.051 eV) and all other active sites. In other words, the Ni NPs altered the absorption energies on the pyridinic N sites, leading to more efficient CO₂ reduction in the case of Ni@Ni–N₄-PD. Although it was not absorbed on the Ni–N₄-GH sites, the COOH* intermediate displayed weak absorption energies on Ni@Ni–N₄-GH (1.648 eV) after the introduction of the Ni NPs. In addition, the ΔG_{H*} of the competing HER (Fig. S32b) corresponded to a higher energy barrier for H* formation on the Ni@Ni–N₄-Ni and Ni@Ni–N₄-N sites, and the free energy barrier of water dissociation was significantly lower on Ni@Ni–N₄-PD, leading to the efficient transformation of H₂O molecules to H* on the Ni@Ni–N₄-PD sites [26]. It has been reported that H* is a key intermediate in the COOH* and CO* formation processes, and thus, the formation of H* during the catalytic process boosted the CO₂RR kinetics [26,59]. Overall, the Ni NPs did not affect the electronic structures of the Ni–N₄ centers but enhanced the electronic density on the uncoordinated N-doped sites, especially pyridinic-N sites, thereby increasing the binding strength of the key reaction COOH* intermediate and resulting in boosted CO₂RR catalysis. These theoretical conclusions coupled with the experimental results demonstrate the effectiveness of uncoordinated N-doped sites and Ni NPs in enhancing the CO₂RR catalysis of Ni–N₄ sites and anticipated to offer ideas and guidelines for the development of high-performance electrocatalysts.

4. Conclusions

A simple low temperature synthesis technique was developed as an alternative to the standard high-temperature method for producing Ni NPs encapsulated in Ni–N–C catalysts with abundant single atomic Ni–N₄ and uncoordinated N-doped sites for effective CO₂ reduction to CO. The effects of Ni NPs on the Ni–N₄ and uncoordinated N-dopes sites, as well as the synergistically improved CO₂RR for hybrid catalysts, were experimentally explored. Comprehensive insights into the mechanism of the synergistic impact were derived through DFT calculations. The findings of the initial screening studies and characterization demonstrated the importance of the high specific surface areas of the electrode in enhancing the reaction rates. The intrinsic activity, which was correlated with the summation of Ni–N₄ and pyridinic N-doped sites, suggested that both Ni–N₄ and pyridinic-N sites functioned as active sites for CO₂RR. Controlled tests and DFT investigations showed that the Ni NPs changed the electron density over the pyridinic N sites, thereby synergistically improving the intrinsic catalytic activity of Ni–N₄ sites by lowering the reaction energy barrier for the rate-determining step of *COOH production. The optimized catalyst achieved high CO₂RR activity with a high FE_{CO} of 97.4% at 0.7 V, as the porous CNT network structures provided highly accessible active site and a fast electron transfer pathway. The high performance was also attributable to the Ni NP modulated electronic structure induced synergistic effect of the Ni–N₄ and N-dopes sites. The proposed Ni-NCNT framework could be extended to synthesize other transition metals with highly exposed M–N_x sites and N-doped sites for various electrochemical reactions such as nitrogen reduction, oxygen reduction, and water splitting.

CRediT authorship contribution statement

Sim Eunji: Methodology, Writing – review & editing. **Kim Tae Kyu:** Conceptualization, Validation, Writing – review & editing. **Reddy K. Arun Joshi:** Data curation, Formal analysis. **Song Inae:** Data curation, Formal analysis. **Eom Yae-eun:** Data curation, Formal analysis. **Boppella Ramireddy:** Conceptualization, Data curation, Formal analysis, Investigation, Methodology, Writing – original draft. **Kim Youngsam:** Data curation, Formal analysis, Methodology.

Declaration of Competing Interest

The authors declare that they have no known competing financial

interests or personal relationships that could have appeared to influence the work reported in this paper.

Data availability

Data will be made available on request.

Acknowledgements

This research was supported by the Basic Science Research Program (NRF-2022R1A2C3003081, 2020H1D3A1A02081461, and 2020R1A2C2007468) through the National Research Foundation of Korea (NRF) funded by the Ministry of Education and Ministry of Science and ICT and the Yonsei University Research Fund (Yonsei Frontier Lab. Young Researcher Supporting Program) of 2020. The authors appreciate Dr. Mani Balamurugan for the help in supporting experiments and fruitful discussions.

Appendix A. Supporting information

Supplementary material related to this article are available free of charge via the internet. Experimental details about sample treatments, MEA electrolysis cell preparations, computational details, and other results of measurements and calculations. Supplementary data associated with this article can be found in the online version at doi:[10.1016/j.apcatb.2024.123699](https://doi.org/10.1016/j.apcatb.2024.123699).

References

- [1] Y.Y. Birdja, E. Pérez-Gallent, M.C. Figueiredo, A.J. Göttle, F. Calle-Vallejo, M.T. M. Koper, Advances and challenges in understanding the electrocatalytic conversion of carbon dioxide to fuels, *Nat. Energy* 4 (2019) 732–745, <https://doi.org/10.1038/s41560-019-0450-y>.
- [2] M.G. Kibria, J.P. Edwards, C.M. Gabardo, C.-T. Dinh, A. Seifitokaldani, D. Sinton, E.H. Sargent, Electrochemical CO₂ reduction into chemical feedstocks: from mechanistic electrocatalysis models to system design, *Adv. Mater.* 31 (2019) 1807166, <https://doi.org/10.1002/adma.201807166>.
- [3] E.V. Kondratenko, G. Mul, J. Baltrusaitis, G.O. Larrazabal, J. Perez-Ramirez, Status and perspectives of CO₂ conversion into fuels and chemicals by catalytic, photocatalytic and electrocatalytic processes, *Energy Environ. Sci.* 6 (2013) 3112–3135, <https://doi.org/10.1039/C3EE41272E>.
- [4] Q.-J. Wu, D.-H. Si, Q. Wu, Y.-L. Dong, R. Cao, Y.-B. Huang, Boosting electroreduction of CO₂ over cationic covalent organic frameworks: hydrogen bonding effects of halogen ions, *Angew. Chem. Int. Ed.* 62 (2023) e202215687, <https://doi.org/10.1002/anie.202215687>.
- [5] W. Ju, A. Bagger, G.-P. Hao, A.S. Varela, I. Sinev, V. Bon, B. Roldan Cuena, S. Kaskel, J. Rossmeisl, P. Strasser, Understanding activity and selectivity of metal-nitrogen-doped carbon catalysts for electrochemical reduction of CO₂, *Nat. Commun.* 8 (2017) 944, <https://doi.org/10.1038/s41467-017-01035-z>.
- [6] A.S. Varela, W. Ju, A. Bagger, P. Franco, J. Rossmeisl, P. Strasser, Electrochemical reduction of CO₂ on metal-nitrogen-doped carbon catalysts, *ACS Catal.* 9 (2019) 7270–7284, <https://doi.org/10.1021/acscatal.9b01405>.
- [7] R. Boppella, M. Austeria P, Y. Kim, I. Song, Y. Eom, D.P. Kumar, M. Balamurugan, E. Sim, D.H. Kim, T.K. Kim, Pyrrolic N-stabilized monovalent Ni single-atom electrocatalyst for efficient CO₂ reduction: identifying the role of pyrrolic-N and synergistic electrocatalysis, *Adv. Funct. Mater.* 32 (2022) 2202351, <https://doi.org/10.1002/adfm.202202351>.
- [8] L. Jiao, J. Zhu, Y. Zhang, W. Yang, S. Zhou, A. Li, C. Xie, X. Zheng, W. Zhou, S.-H. Yu, H.-L. Jiang, Non-bonding interaction of neighboring Fe and Ni single-atom pairs on MOF-derived N-doped carbon for enhanced CO₂ electroreduction, *J. Am. Chem. Soc.* 143 (2021) 19417–19424, <https://doi.org/10.1021/jacs.1c08050>.
- [9] X. Cui, W. Li, P. Ryabchuk, K. Junge, M. Beller, Bridging homogeneous and heterogeneous catalysis by heterogeneous single-metal-site catalysts, *Nat. Catal.* 1 (2018) 385–397, <https://doi.org/10.1038/s41929-018-0090-9>.
- [10] H.B. Yang, S.-F. Hung, S. Liu, K. Yuan, S. Miao, L. Zhang, X. Huang, H.-Y. Wang, W. Cai, R. Chen, J. Gao, X. Yang, W. Chen, Y. Huang, H.M. Chen, C.M. Li, T. Zhang, B. Liu, Atomically dispersed Ni(I) as the active site for electrochemical CO₂ reduction, *Nat. Energy* 3 (2018) 140–147, <https://doi.org/10.1038/s41560-017-0078-8>.
- [11] Y. Hou, Y.-L. Liang, P.-C. Shi, Y.-B. Huang, R. Cao, Atomically dispersed Ni species on N-doped carbon nanotubes for electroreduction of CO₂ with nearly 100% CO selectivity, *Appl. Catal. B Environ.* 271 (2020) 118929, <https://doi.org/10.1016/j.apcatb.2020.118929>.
- [12] S.Y. Liang, Q. Jiang, Q. Wang, Y.F. Liu, Revealing the real role of nickel decorated nitrogen-doped carbon catalysts for electrochemical reduction of CO₂ to CO, *Adv. Energy Mater.* 11 (2021) 2101477. (<https://doi.org/10.1002/aenm.202101477>).

- [13] H. Fei, J. Dong, Y. Feng, C.S. Allen, C. Wan, B. Voloskiy, M. Li, Z. Zhao, Y. Wang, H. Sun, P. An, W. Chen, Z. Guo, C. Lee, D. Chen, I. Shakir, M. Liu, T. Hu, Y. Li, A. I. Kirkland, X. Duan, Y. Huang, General synthesis and definitive structural identification of MN4C4 single-atom catalysts with tunable electrocatalytic activities, *Nat. Catal.* 1 (2018) 63–72, <https://doi.org/10.1038/s41929-017-0008-y>.
- [14] R. Ma, X. Cui, Y. Wang, Z. Xiao, R. Luo, L. Gao, Z. Wei, Y. Yang, Pyrolysis-free synthesis of single-atom cobalt catalysts for efficient oxygen reduction, *J. Mater. Chem. A* (2022), <https://doi.org/10.1039/DITA08412G>.
- [15] P.P. Sharma, J. Wu, R.M. Yadav, M. Liu, C.J. Wright, C.S. Tiwary, B.I. Yakobson, J. Lou, P.M. Ajayan, X.-D. Zhou, Nitrogen-doped carbon nanotube arrays for high-efficiency electrochemical reduction of CO₂: on the understanding of defects, defect density, and selectivity, *Angew. Chem. Int. Ed.* 54 (2015) 13701–13705, <https://doi.org/10.1002/anie.201506062>.
- [16] Z. Zhang, L. Yu, Y. Tu, R. Chen, L. Wu, J. Zhu, D. Deng, Unveiling the active site of metal-free nitrogen-doped carbon for electrocatalytic carbon dioxide reduction, *Cell Rep. Phys. Sci.* 1 (2020) 100145, <https://doi.org/10.1016/j.xcrp.2020.100145>.
- [17] S. Liu, H. Yang, X. Huang, L. Liu, W. Cai, J. Gao, X. Li, T. Zhang, Y. Huang, B. Liu, Identifying active sites of nitrogen-doped carbon materials for the CO₂ reduction reaction, *Adv. Funct. Mater.* 28 (2018) 1800499, <https://doi.org/10.1002/adfm.201800499>.
- [18] X. Wang, S. Ding, T. Yue, Y. Zhu, M. Fang, X. Li, G. Xiao, Y. Zhu, L. Dai, Universal domino reaction strategy for mass production of single-atom metal-nitrogen catalysts for boosting CO₂ electroreduction, *Nano Energy* 82 (2021) 105689, <https://doi.org/10.1016/j.nanoen.2020.105689>.
- [19] W. Ni, Z. Liu, Y. Zhang, C. Ma, H. Deng, S. Zhang, S. Wang, Electrocatalysis of carbon dioxide driven by the intrinsic defects in the carbon plane of a single Fe–N4 site, *Adv. Mater.* 33 (2021) 2003238, <https://doi.org/10.1002/adma.202003238>.
- [20] R. Daiyan, X. Tan, R. Chen, W.H. Saputra, H.A. Tahini, E. Lovell, Y.H. Ng, S. C. Smith, L. Dai, X. Lu, R. Amal, Electroreduction of CO₂ to CO on a mesoporous carbon catalyst with progressively removed nitrogen moieties, *ACS Energy Lett.* 3 (2018) 2292–2298, <https://doi.org/10.1021/acsenergylett.8b01409>.
- [21] N. Leonard, W. Ju, I. Sinev, J. Steinberg, F. Luo, A.S. Varela, B. Roldan Cuenya, P. Strasser, The chemical identity, state and structure of catalytically active centers during the electrochemical CO₂ reduction on porous Fe–nitrogen–carbon (Fe–N–C) materials, *Chem. Sci.* 9 (2018) 5064–5073, <https://doi.org/10.1039/C8SC00491A>.
- [22] Y.J. Sa, H. Jung, D. Shin, H.Y. Jeong, S. Ringe, H. Kim, Y.J. Hwang, S.H. Joo, Thermal transformation of molecular Ni2+–N4 sites for enhanced CO₂ electroreduction activity, *ACS Catal.* 10 (2020) 10920–10931, <https://doi.org/10.1021/acscatal.0c02325>.
- [23] R. Daiyan, X. Zhu, Z. Tong, L. Gong, A. Razmjou, R.-S. Liu, Z. Xia, X. Lu, L. Dai, R. Amal, Transforming active sites in nickel–nitrogen–carbon catalysts for efficient electrochemical CO₂ reduction to CO, *Nano Energy* 78 (2020) 105213, <https://doi.org/10.1016/j.nanoen.2020.105213>.
- [24] Y. Zhang, L. Jiao, W. Yang, C. Xie, H.-L. Jiang, Rational fabrication of low-coordinate single-atom Ni electrocatalysts by MOFs for highly selective CO₂ reduction, *Angew. Chem. Int. Ed.* 60 (2021) 7607–7611, <https://doi.org/10.1002/anie.202016219>.
- [25] W. Ren, X. Tan, C. Jia, A. Krammer, Q. Sun, J. Qu, S.C. Smith, A. Schueler, X. Hu, C. Zhao, Electronic regulation of nickel single atoms by confined nickel nanoparticles for energy-efficient CO(2) electroreduction, *Angew. Chem. Int. Engl.* 61 (2022) e202203335, <https://doi.org/10.1002/anie.202203335>.
- [26] X. Wang, L. Sang, C.-L. Dong, S. Yao, L. Shuai, J. Lu, B. Yang, Z. Li, L. Lei, M. Qiu, L. Dai, Y. Hou, Proton capture strategy for enhancing electrochemical CO₂ reduction on atomically dispersed metal–nitrogen active sites, *Angew. Chem. Int. Ed.* 60 (2021) 11959–11965, <https://doi.org/10.1002/anie.202100011>.
- [27] Q. Lu, C. Chen, Q. Di, W. Liu, X. Sun, Y. Tuo, Y. Zhou, Y. Pan, X. Feng, L. Li, D. Chen, J. Zhang, Dual role of pyridinic-N doping in carbon-coated Ni nanoparticles for highly efficient electrochemical CO₂ reduction to CO over a wide potential range, *ACS Catal.* 12 (2022) 1364–1374, <https://doi.org/10.1021/acscatal.1c04825>.
- [28] M. Jia, C. Choi, T.-S. Wu, C. Ma, P. Kang, H. Tao, Q. Fan, S. Hong, S. Liu, Y.-L. Soo, Y. Jung, J. Qiu, Z. Sun, Carbon-supported Ni nanoparticles for efficient CO₂ electroreduction, *Chem. Sci.* 9 (2018) 8775–8780, <https://doi.org/10.1039/C8SC03732A>.
- [29] W.Z. Zheng, C.X. Guo, J. Yang, F. He, B. Yang, Z.J. Li, L.C. Lei, J.P. Xiao, G. Wu, Y. Hou, Highly active metallic nickel sites confined in N-doped carbon nanotubes toward significantly enhanced activity of CO₂ electroreduction, *Carbon* 150 (2019) 52–59, <https://doi.org/10.1016/j.carbon.2019.04.112>.
- [30] M. Liang, Y. Liu, J. Zhang, F. Wang, Z. Miao, L. Diao, J. Mu, J. Zhou, S. Zhuo, Understanding the role of metal and N species in M@NC catalysts for electrochemical CO₂ reduction reaction, *Appl. Catal. B Environ.* 306 (2022) 121115, <https://doi.org/10.1016/j.apcatb.2022.121115>.
- [31] Z.-J. Zhao, S. Liu, S. Zha, D. Cheng, F. Stutt, G. Henkelman, J. Gong, Theory-guided design of catalytic materials using scaling relationships and reactivity descriptors, *Nat. Rev. Mater.* 4 (2019) 792–804, <https://doi.org/10.1038/s41578-019-0152-x>.
- [32] R. Boppella, J. Tan, W. Yang, J. Moon, Homologous CoP/NiCoP heterostructure on N-doped carbon for highly efficient and pH-universal hydrogen evolution electrocatalysis, *Adv. Funct. Mater.* 29 (2019) 1807976, <https://doi.org/10.1002/adfm.201807976>.
- [33] D. Hursán, A.A. Samu, L. Janovák, K. Artyushkova, T. Asset, P. Atanassov, C. Janáky, Morphological attributes govern carbon dioxide reduction on N-doped carbon electrodes, *Joule* 3 (2019) 1719–1733, <https://doi.org/10.1016/j.joule.2019.05.007>.
- [34] T. Zhang, X. Han, H. Yang, A. Han, E. Hu, Y. Li, X.-q Yang, L. Wang, J. Liu, B. Liu, Atomically dispersed Nickel(I) on an alloy-encapsulated nitrogen-doped carbon nanotube array for high-performance electrochemical CO₂ reduction reaction, *Angew. Chem. Int. Ed.* 59 (2020) 12055–12061, <https://doi.org/10.1002/anie.202002984>.
- [35] J. Meng, C. Niu, L. Xu, J. Li, X. Liu, X. Wang, Y. Wu, X. Xu, W. Chen, Q. Li, Z. Zhu, D. Zhao, L. Mai, General oriented formation of carbon nanotubes from metal–organic frameworks, *J. Am. Chem. Soc.* 139 (2017) 8212–8221, <https://doi.org/10.1021/jacs.7b01942>.
- [36] N.S. Kim, Y.T. Lee, J. Park, J.B. Han, Y.S. Choi, S.Y. Choi, J. Choo, G.H. Lee, Vertically aligned carbon nanotubes grown by pyrolysis of iron, cobalt, and nickel phthalocyanines, *J. Phys. Chem. B* 107 (2003) 9249–9255, <https://doi.org/10.1021/jp0348950>.
- [37] Y. Liu, H. Jiang, Y. Zhu, X. Yang, C. Li, Transition metals (Fe, Co, and Ni) encapsulated in nitrogen-doped carbon nanotubes as bi-functional catalysts for oxygen electrode reactions, *J. Mater. Chem. A* 4 (2016) 1694–1701, <https://doi.org/10.1039/C5TA10551J>.
- [38] R. Chandrabhan Shende, M. Muruganathan, H. Mizuta, M. Akabori, R. Sundara, Chemical simultaneous synthesis strategy of two nitrogen-rich carbon nanomaterials for all-solid-state symmetric supercapacitor, *ACS Omega* 3 (2018) 17276–17286, <https://doi.org/10.1021/acsomega.8b02835>.
- [39] W.Z. Li, J.G. Wen, Y. Tu, Z.F. Ren, Effect of gas pressure on the growth and structure of carbon nanotubes by chemical vapor deposition, *Appl. Phys. A* 73 (2001) 259–264, <https://doi.org/10.1007/s003390100916>.
- [40] G.D. Nessim, M. Seita, K.P. O'Brien, A.J. Hart, R.K. Bonaparte, R.R. Mitchell, C. V. Thompson, Low temperature synthesis of vertically aligned carbon nanotubes with electrical contact to metallic substrates enabled by thermal decomposition of the carbon feedstock, *Nano Lett.* 9 (2009) 3398–3405, <https://doi.org/10.1021/nl900675d>.
- [41] Y. Zheng, Y. Jiao, Y. Zhu, L.H. Li, Y. Han, Y. Chen, M. Jaroniec, S.-Z. Qiao, High electrocatalytic hydrogen evolution activity of an anomalous ruthenium catalyst, *J. Am. Chem. Soc.* 138 (2016) 16174–16181, <https://doi.org/10.1021/jacs.6b11291>.
- [42] W.-J. Ong, L.-L. Tan, Y.H. Ng, S.-T. Yong, S.-P. Chai, Graphitic carbon nitride (g-C3N4)-based photocatalysts for artificial photosynthesis and environmental remediation: are we a step closer to achieving sustainability? *Chem. Rev.* 116 (2016) 7159–7329, <https://doi.org/10.1021/acs.chemrev.6b00075>.
- [43] Y. Cheng, S. Zhao, B. Johannessen, J.-P. Veder, M. Saunders, M.R. Rowles, M. Cheng, C. Liu, M.F. Chisholm, R. De Marco, H.-M. Cheng, S.-Z. Yang, S.P. Jiang, Atomically dispersed transition metals on carbon nanotubes with ultrahigh loading for selective electrochemical carbon dioxide reduction, *Adv. Mater.* 30 (2018) 1706287, <https://doi.org/10.1002/adma.201706287>.
- [44] X. Zou, X. Huang, A. Goswami, R. Silva, B.R. Sathe, E. Mikmeková, T. Asefa, Cobalt-embedded nitrogen-rich carbon nanotubes efficiently catalyze hydrogen evolution reaction at all pH values, *Angew. Chem. Int. Ed.* 53 (2014) 4372–4376, <https://doi.org/10.1002/anie.201311111>.
- [45] C.-Z. Yuan, H.-B. Li, Y.-F. Jiang, K. Liang, S.-J. Zhao, X.-X. Fang, L.-B. Ma, T. Zhao, C. Lin, A.-W. Xu, Tuning the activity of N-doped carbon for CO₂ reduction via in situ encapsulation of nickel nanoparticles into nano-hybrid carbon substrates, *J. Mater. Chem. A* 7 (2019) 6894–6900, <https://doi.org/10.1039/C8TA11500A>.
- [46] R. Boppella, J. Park, W. Yang, J. Tan, J. Moon, Efficient electrocatalytic proton reduction on CoP nanocrystals embedded in microporous P, N Co-doped carbon spheres with dual active sites, *Carbon* 156 (2020) 529–537, <https://doi.org/10.1016/j.carbon.2019.09.082>.
- [47] D.M. Koshy, S. Chen, D.U. Lee, M.B. Stevens, A.M. Abdellah, S.M. Dull, G. Chen, D. Nordlund, A. Gallo, C. Hahn, D.C. Higgins, Z. Bao, T.F. Jaramillo, Understanding the origin of highly selective CO₂ electroreduction to CO on Ni, N-doped carbon catalysts, *Angew. Chem. Int. Ed.* 59 (2020) 4043–4050, <https://doi.org/10.1002/anie.201912857>.
- [48] R. Boppella, W. Yang, J. Tan, H.-C. Kwon, J. Park, J. Moon, Black phosphorus supported Ni2P co-catalyst on graphitic carbon nitride enabling simultaneous boosting charge separation and surface reaction, *Appl. Catal. B Environ.* 242 (2019) 422–430, <https://doi.org/10.1016/j.apcatb.2018.10.018>.
- [49] A.C. Ferrari, Raman spectroscopy of graphene and graphite: disorder, electron–phonon coupling, doping and nonadiabatic effects, *Solid State Commun.* 143 (2007) 47–57, <https://doi.org/10.1016/j.ssc.2007.03.052>.
- [50] C.H. Sung, R. Boppella, J.-W. Yoo, D.-H. Lim, B.-M. Moon, D.H. Kim, J.Y. Kim, Enhanced stability and electrochemical performance of carbon-coated Ti3+ self-doped TiO2-reduced graphene oxide hollow nanostructure-supported Pt-catalyzed fuel cell electrodes, *Adv. Mater. Interfaces* 4 (2017) 1700564, <https://doi.org/10.1002/admi.201700564>.
- [51] R. Boppella, J. Park, H. Lee, G. Jang, J. Moon, Hierarchically structured bifunctional electrocatalysts of stacked core–shell CoS1–xPx heterostructure nanosheets for overall water splitting, *Small Methods* 4 (2020) 2000043, <https://doi.org/10.1002/smtd.202000043>.
- [52] N. Li, D.-H. Si, Q.-j Wu, Q. Wu, Y.-B. Huang, R. Cao, Boosting electrocatalytic CO₂ reduction with conjugated bimetallic Co/Zn polyphthalocyanine frameworks, *CCS Chem.* 5 (2023) 1130–1143, <https://doi.org/10.31635/ccschem.022.202201943>.
- [53] Y. Chen, S. Ji, C. Chen, Q. Peng, D. Wang, Y. Li, Single-atom catalysts: synthetic strategies and electrochemical applications, *Joule* 2 (2018) 1242–1264, <https://doi.org/10.1016/j.joule.2018.06.019>.
- [54] I. Song, Y. Eom, M.A. P., D.H. Hong, M. Balamurugan, R. Boppella, D.H. Kim, T. K. Kim, Geometric and electronic structural engineering of isolated Ni single atoms for a highly efficient CO₂ electroreduction, *Small* 19 (2023) 2300049, <https://doi.org/10.1002/smll.202300049>.

- [55] L. Ye, Y. Ying, D. Sun, Z. Zhang, L. Fei, Z. Wen, J. Qiao, H. Huang, Highly efficient porous carbon electrocatalyst with controllable N-species content for selective CO₂ reduction, *Angew. Chem. Int. Ed.* 59 (2020) 3244–3251, <https://doi.org/10.1002/anie.201912751>.
- [56] K. Mamtani, D. Jain, D. Zemlyanov, G. Celik, J. Luthman, G. Renkes, A.C. Co, U. S. Ozkan, Probing the oxygen reduction reaction active sites over nitrogen-doped carbon nanostructures (CNx) in acidic media using phosphate anion, *ACS Catal.* 6 (2016) 7249–7259, <https://doi.org/10.1021/acscatal.6b01786>.
- [57] Y. Niu, C. Zhang, Y. Wang, D. Fang, L. Zhang, C. Wang, Confining chainmail-bearing Ni nanoparticles in N-doped carbon nanotubes for robust and efficient electroreduction of CO₂, *ChemSusChem* 14 (2021) 1140–1154, <https://doi.org/10.1002/cssc.202002596>.
- [58] X.-M. Hu, H.H. Hval, E.T. Bjerglund, K.J. Dalgaard, M.R. Madsen, M.-M. Pohl, E. Welter, P. Lamagni, K.B. Buhl, M. Bremholm, M. Beller, S.U. Pedersen, T. Skrydstrup, K. Daasbjerg, Selective CO₂ reduction to CO in water using earth-abundant metal and nitrogen-doped carbon electrocatalysts, *ACS Catal.* 8 (2018) 6255–6264, <https://doi.org/10.1021/acscatal.8b01022>.
- [59] W. Zheng, Y. Wang, L. Shuai, X. Wang, F. He, C. Lei, Z. Li, B. Yang, L. Lei, C. Yuan, M. Qiu, Y. Hou, X. Feng, Highly boosted reaction kinetics in carbon dioxide electroreduction by surface-introduced electronegative dopants, *Adv. Funct. Mater.* 31 (2021) 2008146, <https://doi.org/10.1002/adfm.202008146>.
- [60] K. Mamtani, D. Singh, D. Dogu, D. Jain, J.-M.M. Millet, U.S. Ozkan, Effect of acid-washing on the nature of bulk characteristics of nitrogen-doped carbon nanostructures as oxygen reduction reaction electrocatalysts in acidic media, *Energy Fuels* 32 (2018) 11038–11045, <https://doi.org/10.1021/acs.energyfuels.8b01510>.
- [61] Q. Fan, P. Hou, C. Choi, T.-S. Wu, S. Hong, F. Li, Y.-L. Soo, P. Kang, Y. Jung, Z. Sun, Activation of Ni particles into single Ni–N atoms for efficient electrochemical reduction of CO₂, *Adv. Energy Mater.* 10 (2020) 1903068, <https://doi.org/10.1002/aenm.201903068>.
- [62] D.D. Zhu, J.L. Liu, S.Z. Qiao, Recent advances in inorganic heterogeneous electrocatalysts for reduction of carbon dioxide, *Adv. Mater.* 28 (2016) 3423–3452, <https://doi.org/10.1002/adma.201504766>.
- [63] T. Möller, W. Ju, A. Bagger, X. Wang, F. Luo, T. Ngo Thanh, A.S. Varela, J. Rossmeisl, P. Strasser, Efficient CO₂ to CO electrolysis on solid Ni–N–C catalysts at industrial current densities, *Energy Environ. Sci.* 12 (2019) 640–647, <https://doi.org/10.1039/C8EE02662A>.
- [64] C. Liu, Y. Wu, K. Sun, J. Fang, A. Huang, Y. Pan, W.-C. Cheong, Z. Zhuang, Z. Zhuang, Q. Yuan, H.L. Xin, C. Zhang, J. Zhang, H. Xiao, C. Chen, Y. Li, Constructing FeN₄/graphitic nitrogen atomic interface for high-efficiency electrochemical CO₂ reduction over a broad potential window, *Chem* 7 (2021) 1297–1307, <https://doi.org/10.1016/j.chempr.2021.02.001>.
- [65] Z. Zhu, Z. Li, J. Wang, R. Li, H. Chen, Y. Li, J.S. Chen, R. Wu, Z. Wei, Improving NiNN and pyridinic N active sites with space-confined pyrolysis for effective CO₂ electroreduction, *eScience* 2 (2022) 445–452, <https://doi.org/10.1016/j.esci.2022.05.002>.
- [66] T. Asset, S.T. Garcia, S. Herrera, N. Andersen, Y. Chen, E.J. Peterson, I. Matanovic, K. Artyushkova, J. Lee, S.D. Minteer, S. Dai, X. Pan, K. Chavan, S. Calabrese Barton, P. Atanassov, Investigating the nature of the active sites for the CO₂ reduction reaction on carbon-based electrocatalysts, *ACS Catal.* 9 (2019) 7668–7678, <https://doi.org/10.1021/acscatal.9b01513>.
- [67] S. Ni, Z. Li, J. Yang, Oxygen molecule dissociation on carbon nanostructures with different types of nitrogen doping, *Nanoscale* 4 (2012) 1184–1189, <https://doi.org/10.1039/C1NR11086A>.
- [68] A. Dahal, M. Batzill, Graphene-nickel interfaces: a review, *Nanoscale* 6 (2014) 2548–2562, <https://doi.org/10.1039/C3NR05279F>.
- [69] W. Ni, Z. Liu, X. Guo, Y. Zhang, C. Ma, Y. Deng, S. Zhang, Dual single-cobalt atom-based carbon electrocatalysts for efficient CO₂-to-syngas conversion with industrial current densities, *Appl. Catal. B Environ.* 291 (2021) 120092, <https://doi.org/10.1016/j.apcatb.2021.120092>.
- [70] K. Jiang, S. Siahrostami, A.J. Akey, Y. Li, Z. Lu, J. Lattimer, Y. Hu, C. Stokes, M. Gangishetty, G. Chen, Y. Zhou, W. Hill, W.-B. Cai, D. Bell, K. Chan, J.K. Nørskov, Y. Cui, H. Wang, Transition-metal single atoms in a graphene shell as active centers for highly efficient artificial photosynthesis, *Chem* 3 (2017) 950–960, <https://doi.org/10.1016/j.chempr.2017.09.014>.
- [71] Q. Li, W. Zhu, J. Fu, H. Zhang, G. Wu, S. Sun, Controlled assembly of Cu nanoparticles on pyridinic-N rich graphene for electrochemical reduction of CO₂ to ethylene, *Nano Energy* 24 (2016) 1–9, <https://doi.org/10.1016/j.nanoen.2016.03.024>.